Radio Frequency Power Absorption in a Human Model with Pacemakers in MRI

by

Houman Abrishamkar

B.Sc., University of Toronto, 1998
B.A.Sc., University of Ottawa, 2003

A Thesis Submitted in Partial Fulfillment of the
Requirements for the Degree of

MASTER OF APPLIED SCIENCE

in the Department of
Electrical and Computer Engineering

Supervisory Committee

Dr. M.A. Stuchly, Supervisor (Dept. of Electrical and Computer Engineering)

Dr. J. Bornemann, Co-Supervisor (Dept. of Electrical and Computer Engineering)

Dr. A.M. Rowe, Outside Member (Dept. of Mechanical Engineering)

Dr. Y. Coady, External Examiner (Dept. of Computer Science)

Abstract

The interactions of the radio frequency (RF) fields in magnetic resonance imaging (MRI) with a human body model are investigated. In particular, the interactions of these fields with an implanted pacemaker are studied. The specific absorption rate (SAR) levels in a heterogeneous body model are evaluated in two different birdcage coils - a resonant and a non-resonant coil - at a magnetic field of 1.5 T. The enhancement of the SAR due to an implanted cardiac pacemaker and the effect of the conductivity of the pacemaker lead on the SAR levels are investigated. The finite difference time domain (FDTD) technique is used to model these interactions. The SAR levels are found to be low in the heart region, and thus the SAR enhancement due to the pacemaker lead is relatively low. Modeling of the pacemaker leads as perfect conductors results in greater SAR enhancements than those produced by actual conductive leads.

Table of Contents

List of Figures

List of Tables

Glossary of Terms

ABC	Absorbing Boundary Condition
AR	Anti rotational
CR	Co-rotating
FDA	Food and Drug Administration
FDTD	Finite-Difference Time-Domain
FEM	Finite Element Method
FFT	Fast Fourier Transform
MoM	Method of Moments
MRI	Magnetic Resonance Imaging
NMV	Net Magnetization Vector
PEC	Perfect Electric Conductor
PML	Perfectly Matched Layer
RF	Radio Frequency
SAR	Specific Absorption Rate

Acknowledgements

I would like to thank my supervisor, Dr. Maria Stuchly, for her continuous support and guidance. Dr. Stuchly's insights throughout this work have been invaluable, and her willingness to carefully consider every aspect of it has made the project possible. I wish to thank her for her perseverance through the many revisions and reviews.

I would also like to thank Dr. Jens Bornemann for agreeing to be my co-supervisor and advising me throughout this project.

I am grateful to Dr. Kris Caputa for his input, support, and invaluable assistance with the body models. Special thanks should be given to Ms. Donna Shannon for her support, advice, and enthusiasm during the course of this research.

I would like to thank my committee members, Dr. Bornemann, Dr. Coady, and Dr. Rowe, for their helpful suggestions on my thesis.

Finally, I would like to thank my colleagues in the Bioelectric, Optics, and Microwave lab.

To my parents, for their love and support.

1 Introduction

Magnetic resonance imaging (MRI) has become the primary imaging tool in many areas of clinical medicine. With the aid of this technology, physicians can now have a clear picture of internal organs and tissues of patients. These images have a high spatial resolution and are important in treating a broad range of medical conditions including cardiovascular disorders. Physicians are able to closely look at the structure of the heart and major vessels. The size and thickness of the chambers of the heart can be investigated and the extent of damage caused by a heart attack or progressive heart disease can be determined. Some patients with cardiovascular disorders have implanted pacemakers. In certain instances, these patients may be denied an MRI procedure that may considerably affect their health.

1.1 Motivation

Over 2.5 million people living in U.S. have surgically implanted pacemakers [1]. It is estimated that additional 500,000 individuals will undergo pacemaker implantation each year. Traditionally, due to safety concerns pacemaker recipients have been excluded from MRI benefits. A Japanese study in 1999 concluded that 17% of the pacemaker recipients required MRI scans during a one year period. However, they were denied due to the presence of an implanted cardiac pacemaker [1]. Extending this result to the North American population with cardiac pacemaker indicates that a large number of patients will be subject to inferior imaging methods. This is of dire consequence since it may lead to missed diagnosis.

Advances in technology have lead to new-generation cardiac pacemakers with decreased ferromagnetic content, more sophisticated circuitry, and onboard computer capabilities, thus making MRI procedures feasible for these patients [2], [3]. The main limitation is the radio frequency (RF) power deposition, quantified as the specific absorption rate (SAR), and enhanced RF heating of tissues surrounding the pacemaker generator and pacemaker lead. Other investigators have studied the SAR increases and RF heating in saline models and numerical models of the human body with metallic implants [4], [5]. However, there is no previously reported numerical evaluation of a realistic human model with an implanted cardiac pacemaker [5].

Similarly, there are only very limited data on SAR values in various organs of the human body. It is well recognized that higher SAR values for instance in the limbs are not of the same health consequences as high SAR values in some internal organs.

1.2 Objective

The objectives of this research and thesis are:

- To develop a model of a birdcage RF coil representing that used in whole-body MRI scans. This model should be compatible with a numerical technique used.
- To model the interactions of the radiated electromagnetic fields from the RF coil with a realistic human body model using the finite-difference time-domain (FDTD) method.
- To ensure the reliability of the data by comparing the simulation results with published data, where available.

- To evaluate enhanced SAR in a heterogeneous model of a human body with *in situ* pacemaker generator and pacemaker lead in a 1.5 T MRI system (RF equal to 64 MHz).
- To evaluate organ dosimetry in a heterogeneous model of a human body in a 1.5 T MRI system.

1.3 Thesis Outline

Chapter 2 gives a brief overview of the physical concepts involved in magnetic resonance imaging. A concise review of different RF body coils employed in MRI is provided. A detailed description of the birdcage body coil used in this study is given.

Chapter 3 contains a review of the present state of knowledge on MRI safety. Various studies pertaining to the RF heating in body models during MRI scans are presented. Enhanced heating around elongated metallic implant in body models is discussed. The findings from both experimental and numerical approaches are introduced.

Chapter 4 describes the models employed in this study and the computational method. Models of the birdcage RF coil, simple human body models (cylindrical), and a realistic human body model are presented. The numerical method – finite difference time domain (FDTD) method – has been used in this research. The main principles along with various aspects of proper modeling are presented. A software package developed at the University of Victoria based on FDTD code has been used in this work.

Chapter 5 analyzes the performance of the birdcage coils with various loadings for a 1.5 T MR system (RF = 64 MHz). The results of the simulations of the magnetic flux

density in the empty coil and coil loaded with the body models are presented. Using these results and their comparison with the published data, the reliability of our simulation and methodology are assessed.

Chapter 6 investigates the interaction of the electromagnetic fields with a heterogeneous human body model during an MRI procedure. From the FDTD simulation results, the induced SAR levels in the body are evaluated. The SAR values (average and 1g maximum) in various tissues and organs are computed as well. Enhancement of the SAR in tissues and organs due to the presence of a pacemaker generator and its lead is investigated.

Chapter 7 summarizes contributions of the thesis and conclusions that can be drawn regarding effects of the cardiac pacemaker on the increase of the SAR values, and thus the safety of MRI imaging. Suggestions for possible future extension to this work are provided as well.

2 Background Theory

This chapter briefly outlines the basic principles of MRI, whose understanding is necessary for undertaking the research described in this thesis and meeting the objectives outlined in Chapter 1. A more detailed theory can be found e.g. in [6]. Since interactions of RF fields are the subject of this work, performance of coils employed to produce these fields, and more specifically, most often used in practice birdcage coils, are described.

2.1 Basics of Imaging

2.1.1 Nuclear Magnetism

The interaction between an applied magnetic field and a nucleus that possess spin is the basis for magnetic resonance. The nuclear spin angular momentum is an inherent property of an atom and its value depends on the atomic composition. The allowed values for the spin are: zero, half-integer, and integer values. A nucleus with a spin of zero does not interact with an external magnetic field and hence can not be studied using the magnetic resonance. Such nuclei have an even number atomic weight and an even atomic number [7]. Table 2-1 lists the spin and nuclear composition for some atoms commonly found in biological systems. The ^{1}H nucleus is most often used in MR imaging techniques due to its abundance in the human body and its large magnetic moment [8].

Table 2-1: Constants for Selected Nuclei of Biological Interest [7]

Element	Nuclear Composition		Nuclear Spin	Gyromagnetic Ratio γ (MHz T^{-1})	*f* at 1.5 T (MHz)
	Protons	Neutrons			
^{1}H	1	0	1/2	42.58	63.86
^{2}H	1	1	1	6.538	9.803
^{3}He	2	1	1/2	32.44	48.65
^{6}Li	3	3	1	6.266	9.399
^{7}Li	3	4	3/2	16.55	24.82
^{12}C	6	6	0	0	0
^{13}C	6	7	1/2	10.71	16.06
^{14}N	7	7	1	3.077	4.616
^{15}N	7	8	1/2	4.317	6.475
^{16}O	8	8	0	0	0
^{17}O	8	9	5/2	5.774	8.661
^{19}F	9	10	1/2	40.08	60.12
^{23}Na	11	12	3/2	11.27	16.90
^{31}P	15	16	1/2	17.25	25.87
^{129}Xe	54	75	1/2	11.86	17.79

The nucleus rotates about an axis perpendicular to the direction of rotation at a constant rate. This rotating charged particle produces a magnetic field called a nuclear magnetic moment, whose intensity is related to the mass, charge, and rate of spin of the nucleus [9]. The magnetic moment of the nucleus is parallel to the axis of rotation (Figure 2-1).

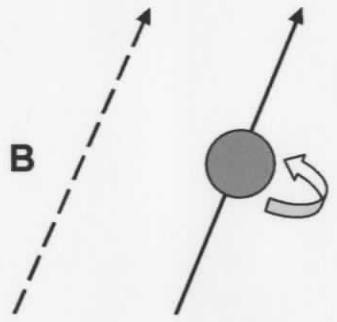

Figure 2-1: A rotating nucleus with a positive charge produces a magnetic field known as the magnetic moment oriented parallel to the axis of rotation [7]

The hydrogen nucleus is most often used in MR imaging. In the absence of an external magnetic field the magnetic moments of the hydrogen nuclei are randomly oriented. In the presence of a strong magnetic field the magnetic moments of the hydrogen nuclei align with the magnetic field. Some of these nuclei are orientated parallel to the magnetic field, and a smaller number of the nuclei are aligned anti-parallel to the magnetic field, as shown in Figure 2-2.

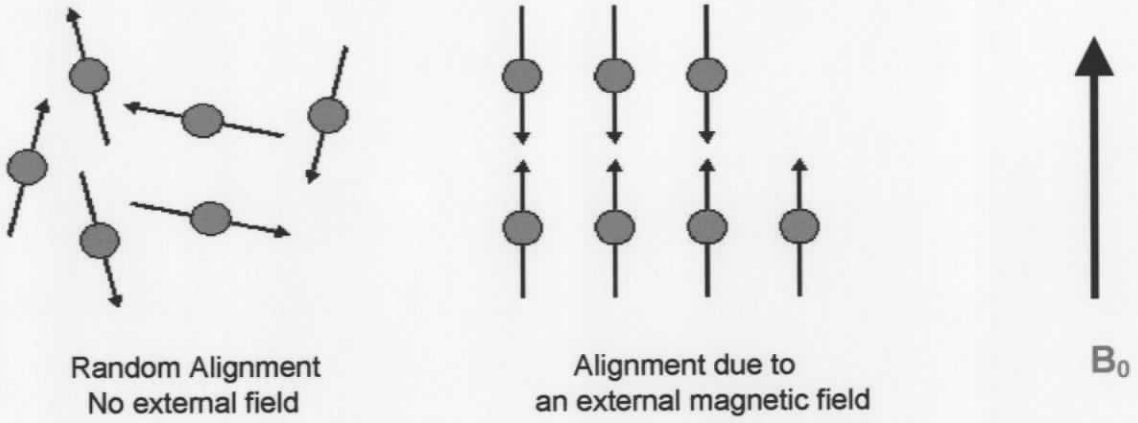

Figure 2-2: Alignment due to the external field [8]

The orientation of the nuclei alignment is determined by the strength of the magnetic field. In the presence of an external magnetic field, a nucleus prefers to be in the lower energy level as it does not posses enough energy to oppose the magnetic field in the anti-parallel direction. This is shown in Figure 2-3.

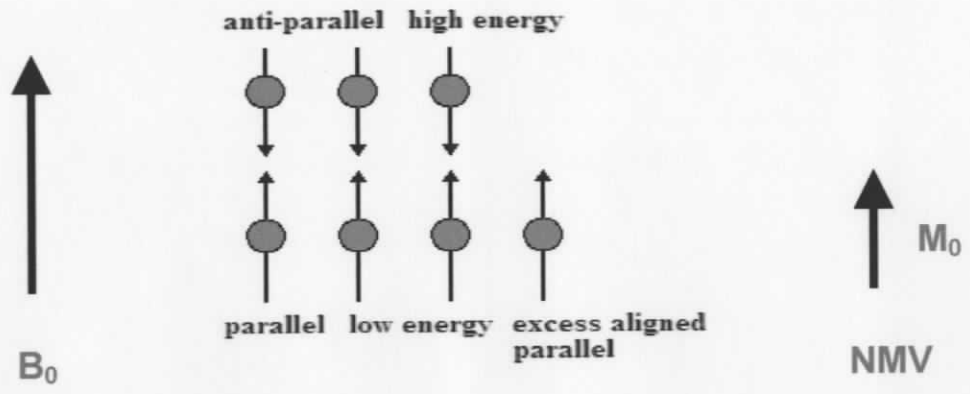

Figure 2-3: The Net Magnetization Vector (NMV) [8]

The magnetic moment of the nuclei aligned parallel to the magnetic field cancel out the magnetic moment of the nuclei in the anti-parallel direction. The unequal number of nuclei in each energy level results in a nonzero vector in the direction parallel to the magnetic field. Hence a tissue abundant with hydrogen nuclei becomes magnetized with a net magnetization value of M_0 in the presence of a magnetic flux density of B_0. The magnitude of M_0 is proportional to B_0:

$$M_0 = \chi B_0 \tag{2.1}$$

where χ is the magnetic susceptibility of the material. This induced magnetization provides the basis for the MRI signal. It is evident from equation 2.1 that increasing the magnetic flux density results in a greater value of M_0 and hence greater MR signal [8].

2.1.2 Precession and the Larmor Equation

When a tissue is exposed to a magnetic field B_0, an additional spin called precession is introduced causing hydrogen nuclei to follow a circular path around B_0. The axis of the

precession is parallel to the main magnetic field $\boldsymbol{B_0}$. This is depicted in Figure 2-4. The precession is due to the interaction of the magnetic field with the spinning nucleus. The frequency of precession – often called the Larmor frequency – is proportional to B_0 and is given by equation 2.2, the Larmor equation:

$$f = \gamma B_0 \tag{2.2}$$

where γ *(Hz/Tesla)* is the gyromagnetic ratio, B_0 *(Tesla)* the static magnetic flux density of the magnet often also referred to as the external magnetic field, and f is the Larmor frequency.

The gyromagnetic ratio is unique for each type of nucleus, and therefore a specific Larmor frequency is associated with a given static magnetic field (magnetic flux density), B_0. Values of γ and the Larmor frequency for $B_0 = 1.5$ T for several nuclei are given in Table 2-1 [7].

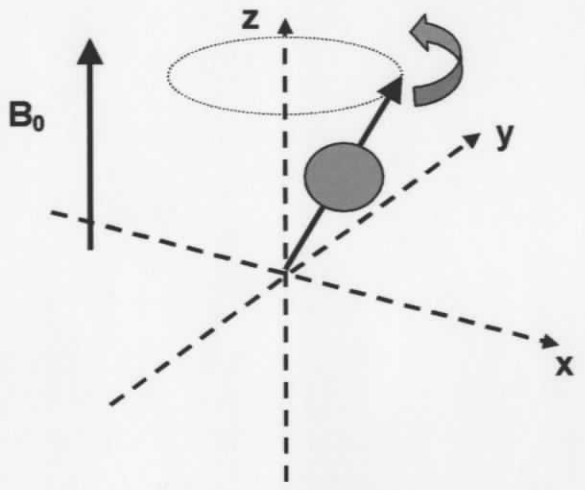

Figure 2-4: Precession due to the interaction of the magnetic field with the spinning nucleus

2.1.3 Resonance

For the resonance to occur, a nucleus has to be exposed to an external RF excitation (B_1-field) with a frequency of oscillation equal to the Larmor frequency. The nucleus only gains this energy and resonates, if the RF magnetic field is perpendicular to the Net Magnetization Vector (NMV) and M_0. As a result of resonance, the NMV is no longer parallel to B_0. The NMV tips away from the z-axis (the axis parallel to B_0) by an angle of α called the flip angle. For a flip angle of 90° the NMV is given enough energy by the RF pulse for the longitudinal NMV to become completely transformed to a transverse NMV (i.e. $M_z=0$ and $M_{xy}= M_0$) and rotating at the Larmor frequency. If a receiver coil is placed in the transverse plane, the MR signal is detected. The MR signal has the Larmor frequency, and its magnitude depends on the amount of magnetization present in the transverse plane [8].

2.1.4 Relaxation T1, and T2, and Free Induction Decay

After the RF source is switched off, the net magnetization vector tends to realign itself with the external magnetic field B_0 and the magnetization vector M_z returns to its equilibrium position. The xy component of the magnetization vector decays at a faster rate than the z component. The increase in M_z is called longitudinal relaxation, T1, and the decay in M_{xy} is termed transverse relaxation, T2. Thus, spin-lattice relaxation (T1) is caused by the excited nuclei transferring their energy to the surrounding lattice and returning to their original state of lower energy and recovering their longitudinal magnetization.

Spin-spin relaxation (T2) occurs due to nuclei exchanging energy with neighboring nuclei. The energy exchange emanates from the interaction of the magnetic fields of each nucleus with its neighbor and it leads to decay or loss of transverse magnetization. The transverse NMV is responsible for the MR signal. After the RF excitation, $\boldsymbol{M_{xy}}$ decreases due to T2 relaxation. As $\boldsymbol{M_{xy}}$ relaxes to zero with a T2 time constant, an electromotive force is induced in the receiving coil due to the oscillating magnetic field. This decaying signal is termed Free Induction Decay (FID), and it is the primary MR signal. The relaxation rate of the nuclei of different tissues varies. This leads to distinct FID signals and consequently different tissue contrast in the image. Using magnetic gradients, the spatial location is determined and the measured signal is transformed to an image via signal processing tools [9].

2.1.5 Magnetic Fields in MRI

A strong static magnetic field, $\boldsymbol{B_0}$, which is uniform over the volume of interest, is necessary in an MRI system. A high $\boldsymbol{B_0}$ field offers better signal to noise ratio and enhanced resolution in spatial domain. A primary field is generated by the main magnet, and gradient coils produce gradient fields that are superimposed on the main field. Gradient fields represent deliberate inhomogeneities introduced in the $\boldsymbol{B_0}$ field. These known inhomogeneities are used to encode spatial information about the returned signal [10].

In the MRI literature, the orientation of B_0 is typically in the z-direction. The total magnetic field is the sum of the B_0 field and the gradient fields (G_x, G_y, and G_z). The

gradient fields are a function of time and space due to on and off switching during the imaging process. To be effective, the gradient pulses must have a period on the order of T2. The total magnetic field in the z-direction is given by:

$$B_{Total}(x,y,z,t) = B_0 + G_x(x,t) + G_y(y,t) + G_z(z,t) \qquad (2.3)$$

As mentioned in Section 2.1.2, the Larmor frequency is determined by the magnitude of the $\boldsymbol{B_0}$ field, which is ideally constant over time and space within a selected volume. Typical magnetic field strengths for the magnets used in clinical MRI for whole body applications range from 0.5 to 3.0 Tesla. MRI systems with higher magnetic field strength (ultra high field) are currently under development.

The magnetic flux density of the pulse generated by RF coils is referred to as the B_1 field with a direction perpendicular to the direction of the primary magnetic field, B_0. The B_1 field is used to induce a flip angle, α, between the net magnetization and z-axis. One component of this field is circularly polarized and rotates at the Larmor frequency. To obtain high quality images, a homogeneous B_1 field must be produced by the RF coil in the volume of interest, so that the nuclei can be excited uniformly. The failure to produce a spatially uniform B_1 field leads to poor image contrast and SNR [10].

2.2 RF Coils and their Characterization

2.2.1 Overview

RF coils are an essential component in a magnetic resonance imaging system [11]. They generate a homogeneous B_1 field at the Larmor frequency in the imaging region. There are three general categories of RF coils: 1) transmit and receive coils, 2) transmit only coils, and 3) receive only coils. Transmit and receive coils function as the transmitter of the B_1 field and receiver of the RF energy. Transmit only coils and receive only coils are used to produce the B_1 field, and to detect the signal from the imaged object, respectively. RF coils are divided into two groups based on their shapes: volume coils and surface coils. Surface coils include single-loop and multiple-loop coils of different shapes. Volume coils include saddle coils and birdcage coils.

In 1980 Ackerman [12] introduced the first surface coil. Surface coils are the simplest design of coil. They are simply a loop of wire that is placed over the region of interest (Figure 2-5). These coils are generally smaller than the volume coils and generate strong and localized magnetic fields. Surface coils relative to volume coils have a higher SNR, since only noise from nearby regions is received [13]. However, due to their poor B_1 field homogeneity they are mainly used as receive coils.

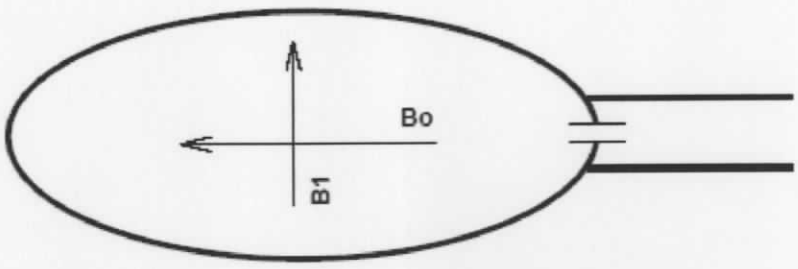

Figure 2-5: A simple surface coil

A saddle coil was first utilized as NMR head coils in 1970 by Ginsberg [14]. Saddle shaped coils are confined to a thin cylindrical shell, are compact and easily constructed (Figure 2-6). They generate a uniform magnetic field in a direction perpendicular to the cylinder axis. Saddle coils are used for both transmission and reception. However, due to their low SNR saddle coils are not used for whole-body scans.

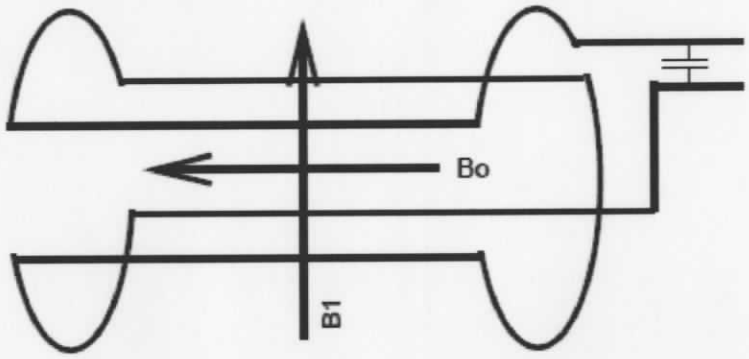

Figure 2-6: Schematic of the saddle coil

Most popular RF coils employed in magnetic resonance imaging are the birdcage coils, first introduced by Hayes *et al.* in 1984 [15]. They can generate a very uniform B_1 field over a large volume within the coil and a better overall SNR than saddle coils. Therefore, they are more often used in clinical systems up to 3 T for whole-body imaging.

2.2.2 The Birdcage Coil

The birdcage coil offers a significantly better B_1 field uniformity and signal-to-noise ratio than the saddle coil, and other specialized coils, e.g., slotted tube resonator and Alderman-Grant coil [15].

Three different configuration of the birdcage resonator are possible: low-pass, high-pass, and band-pass. Each configuration consists of circular ends connected by equally spaced straight segments, as shown in Figure 2-7. Each parallel conductor on the cylindrical surface is referred to as "leg" or "rung" and the term "end-ring" is used to represent the end loop. Depending on the configuration, lumped capacitors are inserted in the gaps in the end-rings and/or the rungs.

Figure 2-7: Configuration of the birdcage resonator

The birdcage resonator can be represented by lumped element equivalent circuits. An element is defined as a closed loop formed with four wire segments: two adjacent legs and two parallel segments from the top and bottom end-rings. Figure 2-8 shows the equivalent circuit model for each of the configurations. Every wire segment is represented as an inductor with L_1 corresponding to the leg segments and L_2 to the end-ring segments. All the inductors L_1 are coupled to each other by mutual inductance; L_2 inductors are mutually coupled as well.

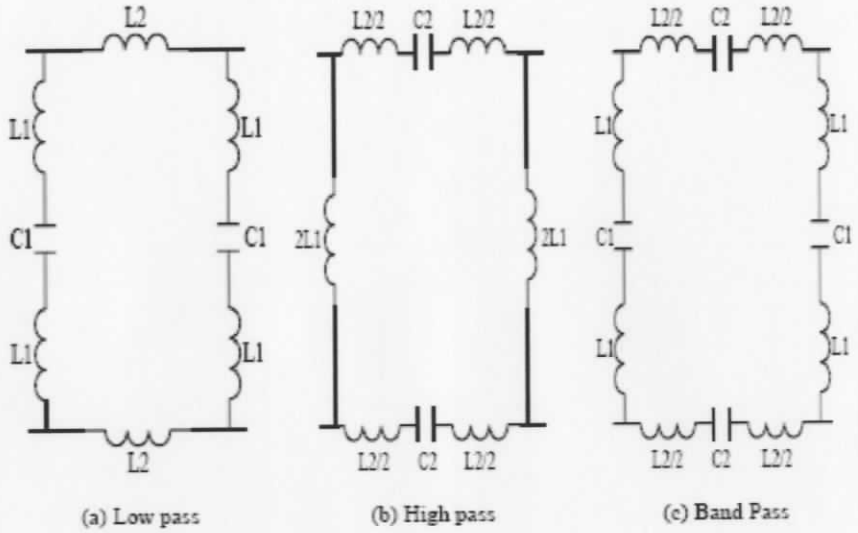

Figure 2-8: Lumped element equivalent circuit of a (a) low-pass, (b) high-pass, (c) band-pass birdcage resonator.

A symmetric *N*-leg high-pass birdcage resonator is formed by using *N* repeated elements of the transmission line shown in Figure 2-8 (b), a portion of which is shown in Figure 2-9. The resonant modes of the birdcage coil can be determined using the circuit analysis [16]. Figure 2-9 shows three segments of a high-pass birdcage coil - a periodic structure with *N*-legs.

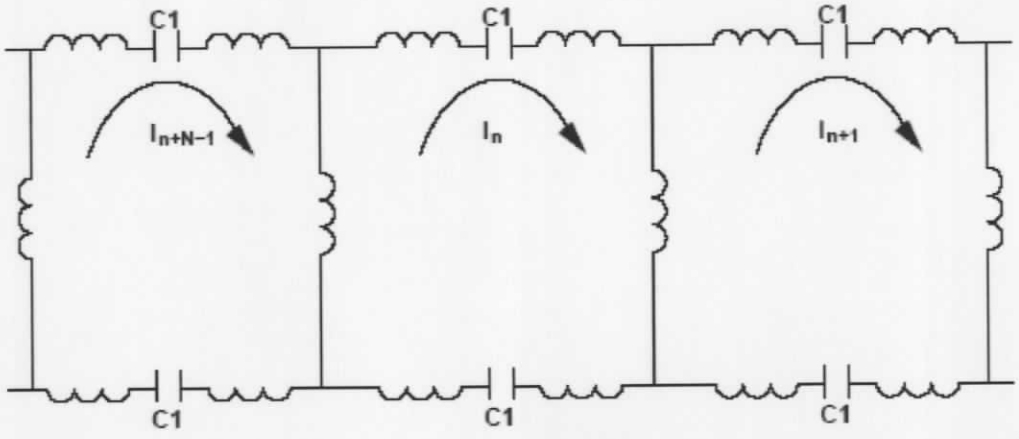

Figure 2-9: Equivalent circuit of a section of a high-pass birdcage resonator.

The Kirchoff's mesh equation in the complex plane for the middle segment containing the current I_n is given by [16]:

$$(j\omega)^2 \sum_{m=0}^{N-1} I_{n+m} M_m + 2I_n \left(\frac{1}{C1}\right) = 0, \tag{2.4}$$

where n varies from 0 to $N-1$, and $n := n + N$, ω *(rad/s)* is the frequency, *C1 (F)* is the value of the lumped capacitor, and M_m *(H)* is the sum of coupling between every parallel pair of conductors in the two meshes with m separation. M_m is determined from [16]:

$$M_m = 2Mleg_m - Mleg_{m-1} - Mleg_{m+1} + 2\left(Mrs_m - Mrs_m^{'}\right), \tag{2.5}$$

where $Mleg_m$ is the mutual inductance between legs and $Mleg_0$ is the self-inductance of any single legs. Mrs_m and $Mrs_m^{'}$ are the mutual inductances between the ring segments in the same and opposite rings, respectively. The resonant frequency of the high-pass birdcage coil is [16]:

$$\omega_k = \sqrt{\frac{2}{C1 \cdot \sum_{m=0}^{N-1} M_m \exp\left(-j2\pi km/N\right)}}, \tag{2.6}$$

where k and m are the integer values from zero to N-1. Resonance occurs at the frequencies for which the propagating waves have an integral number k of wavelengths.

There are two additional modes associated with the high-pass design that cannot be determined from the currents shown in Figure 2-9. These modes are co-rotating (CR) ring mode and anti-rotational (AR) ring mode.

The CR mode is due to equal currents flowing in the same direction in each of the two end-rings. The resonance frequency of the CR mode is [16]:

$$\omega_{CR} = \sqrt{\frac{N}{C1\left(L_{ring} + M_{ring}\right)}}, \tag{2.7}$$

where L_{ring} is the self-inductance of each ring and M_{ring} is the mutual inductance between them. The resonant frequency for the AR ring mode where the end-rings have equal and opposite ring currents and zero leg currents is [16]:

$$\omega_{AR} = \sqrt{\frac{N}{C1\left(L_{ring} - M_{ring}\right)}}. \tag{2.8}$$

A close examination of equations (2.7) and (2.8) indicates that for a negligible mutual inductance the difference in the resonant frequencies for the CR and AR modes are insignificant. In contrast to modes given by (2.6) these modes produce no transverse magnetic field in the center of the birdcage resonator.

The ideal mode of operation for a birdcage coil is in mode 1 where the birdcage elements carry a sinusoidal current distribution. A sinusoidal current distribution in the coil elements results in the coupling between the coil currents and the object (human body or its model) imaged. The current distribution in the coil is given by [17]:

$$I_i = I_{\max} \cos\frac{(i-1)\pi}{N}, \tag{2.9}$$

where I_i is the current in the ith element, I_{max} is the maximum current, and N is the number of current elements. Equation (2.8) is only valid when the coil is small compared to a wavelength. As the length of the coil approaches a quarter wavelength and/or the coupling between the coil and the object becomes significant, equation (2.9) begins to fail.

2.3 Evaluation of Power Absorbed (SAR) in the Human Body

2.3.1 Interaction Mechanism

Applying an external time-varying field to biological tissues displaces the bound charges and orients polar molecules in the direction of the field giving rise to a volume polarization density **P**. At low frequencies, volume polarization density and the applied electric field **E** are in phase. However, as the frequency is increased the charged particles resist acceleration by the changing field, preventing the polarization **P** to keep in phase with the applied field. The applied field loses power due to the work done against the frictional damping forces. This lost power is deposited in the tissue as heat [18].

The polarization **P** is expressed as:

$$\mathbf{P} = \hat{\varepsilon}\chi_e \mathbf{E} \tag{2.10}$$

where $\hat{\varepsilon}$ is the complex permittivity and χ_e is the complex electric susceptibility.

The interactions of the electric field with matter is described in terms of the complex permittivity:

$$\hat{\varepsilon} = \varepsilon' - j\varepsilon'' = \mathbf{D}/\mathbf{E} \qquad (2.11)$$

where **D** is the electric flux density, ε' is the dielectric constant, and ε'' is the loss factor. The dielectric constant ε' is indicative of the ability of the material to store electric field energy, and the loss factor ε'' denotes the energy dissipated in the material. The frictional damping and ohmic losses are included in the loss factor ε''.

When a dielectric is excited at high frequencies with an alternating field **E** an alternating current density $\omega\varepsilon''\mathbf{E}$ flows. This leads to an instantaneous power dissipation of $\omega\varepsilon''|\mathbf{E}|^2$ in units of Wm^{-3} [18]. The relationship between the loss factor ε'' and the conductivity of the material $\sigma(S/m)$ is described by:

$$\sigma = \omega\varepsilon'' \qquad (2.12)$$

Magnetic resonance imaging utilizes electromagnetic fields emitted by an RF coil to construct an image of the internal organs of patients. An important factor in MRI coil design at high frequency is the RF power absorption by patients. The interaction of RF fields with tissues of patient's body raises concern for the safety of the patient. There has been extensive research on the health hazards of RF exposure and guidelines on the safe levels of exposure have been established [19]. Of critical health concern is the induced rise in temperature caused by the RF power deposition. Specific absorption rate (SAR) is a measure of the localized heating of tissues and is given by:

$$SAR = \frac{\sigma|E|^2}{2\rho} \qquad (2.13)$$

where σ (S/m) is the conductivity and ρ (kg/m^3) is the mass density of the tissue, and $|E|$ (V/m) is the magnitude of the electric field in the tissue. By evaluating SAR within specific tissues, safety of a given exposure to RF can be evaluated.

2.3.2 Numerical Evaluation of SAR

The SAR is directly proportional to the square of electric field magnitude within the tissues (equation 2.13). The electric field within the tissues is determined using numerical methods. In MRI imaging repetitive RF pulses are used, thus the SAR is often expressed as

$$SAR = \frac{\sigma |E|^2}{2\rho} \frac{T_e}{T_r} \tag{2.14}$$

where T_e and T_r are the pulse duration and repetition time, respectively.

SAR values in the body model are calculated from the FDTD data as:

$$SAR = \frac{1}{N} \sum_{n=1}^{N} \left(\frac{\sigma_{xn} E_{xn}^{\ 2}}{2\rho_{xn}} + \frac{\sigma_{yn} E_{yn}^{\ 2}}{2\rho_{yn}} + \frac{\sigma_{zn} E_{zn}^{\ 2}}{2\rho_{zn}} \right) \tag{2.15}$$

where summation is over all N voxels in the volume of interest, and σ and ρ represent the conductivity and density of the Yee cell elements (tissue) oriented in the x, y, and z directions at the nth location.

Typically, SAR values are presented for a circularly polarized $\boldsymbol{B_1}$-field in the coil center of a magnitude of 1.957 μT, representing a 3 ms pulse at the center of the coil.

3 Literature Review

Deposition of RF power in human tissue occurring during MRI procedure is specified in terms of the specific absorption rate (SAR). A review of the published literature on the subject is given, and subsequently used for comparison of some of the data computed in the thesis. Similarly, the state of knowledge on the interactions of RF with implants in general and cardiac pacemakers in particular is outlined. This information allowed for identification of the limitations of the knowledge at the commencement of this research, and thus contribution of new knowledge with the results presented in the thesis.

3.1 SAR in the Human Body

The SAR distribution in models of patients during an MRI exam has been the subject of a number of studies [20]-[30]. Realistic human head and body models have been used when modeling the interaction of the electric field in an MR system. The finite-difference time-domain (FDTD) method has been used by most researchers for evaluating SAR levels during MR examination. Although the FDTD method remains the method of choice [23]-[30] for this type of problems, few researchers have used the Finite Element Method (FEM) [20], [21], and [22].

One of the earliest SAR evaluations was performed by Jin et al. [23], who developed a numerical method to investigate the electromagnetic field interaction with the human head for MRI applications. The method employed the biconjugate gradient algorithm (BCG) together with the Fast Fourier Transform (FFT) to solve integro-differential equations. Electromagnetic fields inside a 2 mm high resolution, anatomically detailed model of a human head were computed. The head model was constructed from a series

of MR images. The birdcage coil used had a radius of 20 cm and a length of 40 cm, and consisted of 32 rungs. The computations were performed for both linear and quadrature excitation of the birdcage coil. The magnetic flux density in an empty coil and loaded with a human model, and the SAR values in the model were calculated at 64 MHz, 128 MHz, and 256 MHz, corresponding to the RF frequencies of 1.5 T, 3 T, and 6 T MRI systems. All SAR results were normalized with respect to the maximum value at 64 MHz. The highest SAR values were measured in the parts of the head (skin and muscle) close to the rungs of the birdcage coil at all three frequencies. A linear excitation at 64 MHz produced a maximum SAR of 1 W/kg and 0.57 W/kg in the skin and the muscle respectively. Compared with the linear excitation, the average SAR values using a quadrature excitation were reduced by a factor of about 2 and the maximum SAR values were reduced by a factor of about 3.

Ibrahim et al.[24], [25] also determined a significant reduction in peak SAR values for the quadrature compared to linear excitation, and for the four-port excitation compared to quadrature excitation. A maximum SAR of 0.28 W/kg and 0.24 W/kg were measured in the skin and the muscle tissues, respectively. For the same current in the coil, SAR increased by a factor over 5 at 128 MHz, and at 256 MHz by a factor over 10, compared to that at 64 MHz. The normalization used in this work, makes the results not suitable for comparison with other data.

An evaluation of the electric-field distribution and SAR in a human head model during MRI using the FDTD method was done by Nguyen et al. [26]. A 3-D head/shoulder model (3 mm resolution) of a human, based on images provided by the visible human database project was used. The birdcage coil was modeled with 12 equally spaced rungs

with a diameter of 39.6 cm and a length of 30.3 cm. The computations were performed for a quadrature excitation of the coil. All data were normalized to the average magnetic field inside the coil of 1.957 μT. The SAR was calculated for a frequency range from 63 to 500 MHz. AT 63 MHz, a maximum SAR of 0.95 W/kg was reported in the muscle tissue and an average SAR of 0.20 W/kg in the skin. Nguyen et al. [26] also reported the same phenomenon as Jin et al [23], namely an increase in the SAR values with frequency varying from 63 to 500 MHz.

The FDTD method in combination with the Method of Moments (MoM) was employed by Chen et al. [27] to analyze the B_1 field and SAR in a realistic human head model in shielded RF coils. The MoM was used for computation of the current distribution in the coil and the FDTD method to evaluate the electric and magnetic fields produced by the current. A high-pass birdcage coil made of 16 elements with a length of 26 cm and a diameter of 26 cm was used. The head model with a resolution of 2 mm was constructed from MRI images. The coil was shielded by a cylindrical shield with a diameter of 32 cm and a length of 32 cm. Computations were performed at 64, 128, 171, and 256 MHz. High SAR values were noted over the entire head at 64 MHz; however, with increasing frequency of operation, the high SAR levels tended to concentrate in the deeper region of the head. An increase in the frequency resulted in a deterioration of the B_1 field homogeneity. These results are in agreement with [23].

Collins and Smith [28] performed calculations of SAR in the head, and total power absorbed in the head at frequencies between 64 and 345 MHz. An anatomically-accurate head model with a resolution of 2 × 2 × 2.5 mm was used (the National Library of

Medicine's Visible Male Project). The FDTD method was used to calculate all electrical and magnetic fields throughout the head model in a birdcage coil. The birdcage coil with a diameter of 30 cm had 12 rungs of a length of 25 cm. The coil was excited with equal-amplitude voltage source at the centre of each leg and in the middle of each end ring segment. All SAR values were normalized to 1.957 μT at the centre of the coil for all frequencies. Average SAR and maximum SAR (averaged over 1g) in the head were reported to be 0.178 W/kg and 0.875 W/kg, respectively. In a similar study, using the same head model in a saddle coil model, Collins and Smith [29] calculated SAR. Higher values of SAR, an average SAR of 0.93 W/kg, and maximum SAR of 6.8 W/kg were computed.

Only a few evaluations have been performed for larger coils and imaging of the human torso. Collins and Smith [30] evaluated the B_1 field patterns, SAR, and SNR as functions of frequency for a surface coil placed against the human chest. An anatomically-correct body model (5 mm resolution) created from the National Library of Medicine's Visible Male Project was used. A circular surface coil with a diameter of 22.9 cm was modeled near the chest of the whole-body model. The FDTD method was employed for all the calculations. The results were normalized to 1.957 μT at the centre of the heart. High SAR levels were noted in the chest of the human body model where it was at a close proximity to the coil elements. A whole-body average SAR of 0.14 W/kg and a maximum 1g SAR of 15.24 W/kg was reported at 64 MHz.

Representative computations of SAR in the human torso model are those reported in [5] and [30]. A summary of those results and the representative results for the head is given in Table 3-1.

The main observations from the published data, as outlined and summarized in Table 3-1, are:

- Better magnetic field homogeneity is obtained with a phase-shifted excitation in multiple rungs or sections of the end-ring: The more points of excitation, the better the uniformity.
- Values of the SAR are lower for the birdcage exposure than for other coils for similar coil dimensions and head models.
- Resonant birdcage coils produce lower SAR values than non-resonant coils of the same dimensions.
- The average and maximum SAR values increase with frequency.
- The maximum SAR values occur at the body periphery for the torso in birdcage coils.
- There is paucity of data on SAR in the human torso that can be scaled to various exposures, due to artificial normalization used in some reports.
- There are only limited reliable data on the average and 1g maximum SAR values in various organs of the human body.

Table 3-1: Summary of the Published Results

		Model 1 [23]	Model 2 [23]	Model 3 [26]	Model 4 [28]	Model 5 [29]	Model 6 [30]	Model 7 [5]
Coil Characteristics	RF Coil Type	Birdcage Head Coil	Birdcage Head Coil	Birdcage Head Coil	Birdcage Head Coil	Saddle Head Coil	Surface Body Coil	Birdcage Body Coil
	Length (cm)	40	40	30.3	25	-	-	70
	Diameter (cm)	40	40	39.6	30	-	22.9	70
	Number of rungs	32	32	12	12	-	-	16
	Excitation	Linear	Quadrature	Quadrature	in the legs and the end-rings	-	Four-port	Midpoint of all 16 rungs
Model and Method	Numberical Method	BCG-FFT	BCG-FFT	FDTD	FDTD	FDTD	FDTD	FDTD
	Body Model	Head	Head	Head	Head	Head	Torso	Torso
	Resolution (mm)	2	2	3	$2 \times 2 \times 2.5$	$2 \times 2 \times 2.5$	5	5
Reported Results	Normalization	maximum value at 64 MHz	maximum value at 64 MHz	1.957 μT	1.957 μT	1.957 μT	1.957 μT	1 W/kg
	SARave (W/kg)	0.04	0.02	-	0.18	0.93	0.13	-
	SARmax(W/kg)	1	0.28	0.95	-	-	-	16.5
	1g SARmax (W/kg)	-	-	0.51	0.88	6.84	15.24	-

3.2 Implants in MRI

Electrically conducting implants affect the RF electric fields produced in the human body by the MRI. They can enhance the fields locally, typically producing elevated fields in the tissues near the implant. This results in a greater SAR and corresponding heating in those tissues. The RF field may also directly interfere with the operation of active implants such as cardiac pacemakers. In the past, pacemaker recipients have been excluded from MR imaging. However, new developments have led to new-generation cardiac pacemakers with decreased ferromagnetic content, more sophisticated circuitry, and onboard computer capabilities thus making MRI procedures feasible for these patients [2], [3].

3.2.1 Simplified Implant models

Several investigations have been performed to determine SAR and/or temperature increases due to various implants [22], [31]-[36]. Models of implants included simple metallic rods [5], as well as more realistic representations of actual devices [22], [31]-[36]. Two approaches to the evaluation of implants have been employed, namely numerical modeling and experimental measurements. Some studies used a realistic model of the human body or head, and simulated the electric fields with the FDTD method. Also, at least one investigation evaluated the temperature increases using the bio-heat equation [26].

Ho [5] studied the enhanced SAR in tissues in the vicinity of metallic implants in patients undergoing MRI scans. SAR distributions in a realistic model of the human body were

evaluated using the FDTD method. The model was derived from the National Library of Medicine's Visible Human Project. The simulations were performed for the body with metallic implants exposed to RF magnetic fields at 64 MHz produced by a birdcage coil. Metallic implants with different shapes (cylindrical or L-shaped) and sizes were implanted at different locations in the body model. Similarly to others he found that maximum SAR values occurred at the body periphery. The SAR value near a cylindrical shaped metallic implant (diameter: 1 cm and length: 8 cm) placed near the heart region was 2.0 W/kg, compared to the value of 1.8 W/kg at the same location in the model without the implant. A larger implant with a length of 24 cm and a diameter of 1 cm showed no apparent enhanced SAR in the same region. An L-shaped metallic implant with a diameter of 1 mm was implanted in the base of the spinal column. There was a considerable increase in heating near the tip of the vertical section of the implant. A 1g SAR value of 26.3 W/kg was noted at the vertical tip of the wire. The SAR values for various lengths of 1 cm and 1 mm diameter metallic implants were also investigated. The implants were near the heart, left side of the body, and right side of the body corresponding to regions of low, medium, and high SAR values respectively. The 1 g SAR value at the tip of the 1 cm diameter metallic implant of length 0.24 m was 3.9 W/kg near the heart and 17.6 W/kg in the right side of the body. A 1 gram SAR value of 4.9 W/kg and 32.6 W/kg were reported in the same area – the heart and the right side of the body – for a 1 mm diameter metallic implant of length 0.24 m, respectively. In general, no considerable SAR increase occurred in the low SAR regions. However, in the medium and high SAR value regions, significant amount of heating was noted near

the tip of the metallic cylindrical implants. The amount of heating varied depending on the length of the metallic implant.

Ho [5] established that during an MRI procedure enhanced heating of the tissues due to the presence of metallic implant is contingent on the dimensions, orientation, shape, and location of the metallic implant in the patient. This investigation produced a lot of quantitative data; however, due to the data normalization used (whole-body average SAR); these data can not be used for comparison with results of other studies.

Smith et al. [22] used a General Electric birdcage coil at 64 MHz. A flat rectangular plastic model, 0.52 m wide and 0.71 m long, filled with gel material (a thin layer) of muscle properties was used as the body model. The heating around wires of various lengths and insulation thicknesses in the body model was examined. The duration of RF exposure was 15 minutes. Temperature measurements were made using a Luxtron 790 Fluoroptic Thermometer. Copper wires with thin varnish insulation with lengths varying from 5 to 40 cm were used to examine the effect of the wire length on induced heating. For a 20 cm (0.36λ) long wire a temperature rise of 7°C after 15 minutes of exposure was measured at the tip. This was about seven times greater than the background increase in temperature. This enhanced heating was less pronounced for longer and shorter wires. Computer simulations of heating at the ends of wires were also performed using the finite element method. The simulation results agreed with the experiments. Tests performed on wires covered with a thicker insulation (thickness 0.6 mm and 5 mm of the ends exposed) indicated that increasing the thickness decreased the capacitive coupling to the phantom and less current could leak out along the length of the wire. This in turn resulted in the induced currents to be concentrated at the ends of the wire, causing a

greater temperature rise. The findings in this study represented the worse case estimation of temperature rise, since the effects of blood flow were not considered.

Chou et al. [31] studied the RF heating of an implanted spinal fusion stimulator on a full-size human model in a 1.5T GE Signa 4X MR system. The model included bone, brain, lungs, and muscle. The conditions that were simulated were an intact implant, one wire broken, electrodes only, and no implants as a reference. Fiber optic sensors were used to record changes in the temperature. With the implant intact the maximum temperature rise at the centre of the generator was less than 2°C and at the electrodes less than 1°C. This measurement was taken for a scan time of 26 minutes, corresponding to a whole-body averaged SAR of 1.095 W/kg for a body weight of 68 kg. After a 4 minute scan (whole-body average SAR of 0.914 W/kg), a broken generator lead produced a maximum temperature increase of 11°C at the point where the broken lead connects to the stimulator with the opposite end only experiencing only a 3°C rise. A temperature rise of 1.5°C at one of the electrode pins was measured when the generator and the leads were removed. With the implant removed a temperature rise of less than 0.5° C was measured. The effect of blood flow was not simulated. The study therefore provided a worst-case estimation for the maximum temperature rise. It was concluded that MRI procedures were unsafe for patients wearing a spinal fusion stimulator with a broken lead.

Using a gelled saline model, Nyenhuis et al. [4] measured the temperature rise in the vicinity a Medtronic IsoMed 8472-60 infusion pump and Medtronic SynchroMed 8617L-18 in a 1.5T MR system (GE Signa). The MR exposure time was 20 minutes and resulted in a SAR of 0.95 W/kg in a 34-kg model (saline solution and Polyacrylic acid

gelling agent). The implant was placed in the abdominal region of the body model centered in the axis of the coil. Temperature measurements were taken using a Luxtron 790 Fluroptic thermometer. The maximum temperature rise in the area surrounding the implant was about 0.7° C. It was concluded that patients with the IsoMed pumps were not at risk during an MRI procedure. Also, it was found that heating near the medical implant was due to the induced currents in the tissue rather than the currents in the device. This study did not account for the effect of blood flow on heat transfer.

Heating around a Terumo standard angiography guide wire was examined in two investigation [32], [33]. The wire had a nickel-titanium tapered core, and the surface was coated with a thin layer of hydrophilic polymer. The wire was immersed in a saline bath placed in a 1.5 T Philips Gyroscan NT scanner using a gradient echo sequence with a maximum allowable SAR of 3.9 W/kg. The increase in temperature at the tip of the guide wire was measured. A rise in temperature at the lead tip from 26°C to 74°C occurred after 30 seconds of scanning [32]. Considerable amount of heating was also measured at the wire contact with body tissues. The experiments in [33] were performed in a 1.5 T whole-body MRI system (MAGNETOM Symphony). All experiments were conducted for a maximum whole-body SAR of 1.28 W/kg simulating the worst-case situations. The wire was routed through a model filled with saline solution simulating the tissue. A 34°C increase in temperature was measured at the tip of the wire. Similar results were obtained by Park et al. [34].

Nitz et al. [33] established the influence of the length of guide wire on the induced voltage from the tip of the wire into the tissue. A 6°C and 2°C temperature rise was

observed for a 1.56 m and 1.7 m long guide wires, respectively. For a 1.16 m long wire, the change in temperature dropped to 1°C. The variations in temperature changes were due to resonances occurring at different wire lengths.

Shellock [35] studied the MRI-related heating of seven different passive neurosurgical implants (BioMesh, burr hole covers, cranial screws, and BioClips) using a gel-filled phantom at 1.5 T (GE Signa MR system). A 0.6°C rise in temperature was recorded after 15 minutes of MRI exposure at a SAR of 1.4 W/kg. He concluded that patients with such implants could safely undergo MRI procedures using MR systems with static field intensity of 1.5 T.

Experimental studies were typically preformed using conventional MR systems with human torso models. Hence, the temperature increases inside the body model due to MRI exposure represented those in the clinical conditions. Since the body models were not a realistic representation (saline models with electrical properties resembling those of the human body) of the human body, measurements such as organ dosimetry were not possible. Numerical models of the human body were on the other hand anatomically correct and power deposition and hence SAR in individual organs could be readily evaluated.

Both the numerical modeling and the experimental approach gave insight on the worst-case scenario. In all cases, heat transfer mechanisms such as conduction, and convections (intravascular blood flow and myocardial perfusion) were not accounted for. High SAR values in regions of high perfusion could translate into a lower temperature increase, whereas in areas with nominal perfusion the rise in temperature can be higher for a

relatively low SAR levels. These physiological parameters should therefore be considered when doing full-scale risk analysis.

Experiments and numerical modeling revealed enhanced heating in body models with medical implants during MRI scans. The SAR was maximum in tissues near the periphery of the body near the edges of the body coil; lower SAR values were inside the body. The presence of medical implants caused an increase in heating in the tissues surrounding the implant. The magnitude of heating corresponded to the location, with implants near the surface of the body experiencing higher SAR values than those inside the body. Electrically conductive, elongated implants similar to pacemaker leads, generated heat at and in close proximity of the tip of the wire due to interactions with the electric component of the RF field.

3.2.2 Interactions with Cardiac Pacemakers

Sommer et al. [3] studied the safety of patients with implanted cardiac pacemakers in MRI at 0.5T (Philips Gyroscan T5II). The imaging time was 10 minutes. Both in vitro and in vivo studies were carried out. There was no reported pacing dysfunction and no changes occurred in the program of the pacemaker in the devices tested in vivo and in vitro. In vitro studies were performed with electrodes inserted into the right ventricular septum of a porcine heart, connected to a pacemaker, and immersed in a saline bath (60 × 40 × 25 cm). Forty-four pacemaker leads were investigated. Their lengths were not reported. Maximum RF-induced heating occurred at the electrode-tissue boundary. At an average specific absorption rate of 0.6 W/kg the maximum rise in temperature at the lead tips were 8.9°C measured in vitro. Under a worse-case RF heating condition with a

SAR of 1.3 W/kg, the maximum rise in temperature at the lead tips was 23.5°C. The results presented did not consider the effects of heat transfer due to intravascular blood flow and myocardial perfusion.

An experimental study of induced heating for different pacing electrodes was performed by Achenbach et al. [36]. A 1.5 T Siemens Magnetom MRI system was used. The scan time was 90 seconds. Twenty five different electrodes of various lengths ranging from 48 to 116 cm were considered. The electrodes were inserted into a deep cut in the left ventricle of an isolated porcine heart with the opposite end either in air or in a saline model. An optical temperature sensor was connected to the electrode tip. The study was carried out when the electrodes were connected and when disconnected from a cardiac pacemaker for both monopolar and bipolar electrodes. Overall, the rise in temperature at the electrode tip was less pronounced when the electrode was connected to the pacemaker and immersed in a saline solution. In the case of the monopolar electrodes, the maximum rise in temperature at the tip of the electrode was 5.7°C in air and connected to a pacemaker, and 3.7°C in saline and connected to a pacemaker. For bipolar electrodes, a temperature rise of 3.3°C in air and connected to a pacemaker, and 8.9°C in saline and connected to a pacemaker was measured at the tip of the electrode.

3.3 Summary and Conclusions

Three fields employed in MRI systems, namely static magnetic, gradient magnetic (low frequency), and RF are capable of interactions with cardiac pacemakers. These interactions may result in a health hazard to the person with a pacemaker, who is undergoing an MRI scan. In modern pacemakers the interactions with the static and low

frequency magnetic fields have been eliminated by use of non-magnetic metals (no interaction with the static field) and improved electronics (no interaction with the gradient fields). Thus, the only interaction that may pose health hazard is due to the RF fields.

Human tissues are conductive dielectrics and are heated by RF fields. Excessive heating poses a health hazard. There are various published guidelines aimed at prevention of this hazard. The limits are prescribed in terms of the RF power deposited in a unit mass and are referred to as the specific absorption rate (SAR). Limited number of investigations has been reported, in which SAR distributions in the human body have been evaluated for various MRI coils. These investigations have been performed simulating exposures of relatively advanced models of the human body by numerical methods. Among the most advanced and convenient tools is the FDTD method, which is compatible with voxel models of the human body. Typically the average and maximum 1g SAR values have been reported, but only few studies provided SAR for body organs. Furthermore, normalization of the data is often ambiguous, or not suitable for intercomparison.

Metallic implants, and thus cardiac pacemakers, enhance SAR in their vicinity. Numerical simulations have been performed for simple rods, loops or other simplified representations of actual implants, as well as few specific implants. Modern cardiac pacemakers have only been evaluated experimentally in simplified models of the human body. Therefore, to be able to reliably comply with the guidelines on the SAR, it is necessary to evaluate electric fields from RF field produced by MRI coils by simulating exposure of a human model that has the pacemaker in situ.

Since the birdcage coil is the most popular and advantageous coil for volume scans of the human torso, it is selected for evaluation in this thesis. As previously, the FDTD method is seleced. A voxel human body model with a model of the pacemaker with its leads inserted in a realistic location is used in the simulations performed in the thesis. An evaluation with the pacemaker and its leads in a proper placement is essential in view of the data from previous modeling indicating strong dependence on the position of the implants in the body.

4 Models and Method

To assess the interactions of the RF fields radiated from MRI systems with the human body, numerical models of the RF coil and the human body were employed. A birdcage body coil was used for all the computations. It was selected because of its advantages outlined in Chapter 2. Three body models were employed: cylindrical models representing a simple human body, and two anatomically correct body models. The field solver based on the finite-difference time-domain (FDTD) method, which was previously developed at the University of Victoria, was used.

4.1 Birdcage Coils and their Excitation

Two birdcage body coils were numerically modeled: a non-resonant coil (representing ideal conditions – the best magnetic field uniformity) and a high-pass birdcage resonator (used in practical systems). The birdcage coil was modeled with its length parallel to the z-direction in the FDTD space and the end-rings were in the x-y plane. The coils consisted of sixteen equally spaced rungs forming a cylinder. Circular rings were attached to the top and bottom of the open cavity. The circular rings in the high-pass configuration contained gaps at mid-points between the rungs where lumped capacitors were inserted. Both coils had a diameter and a length of 0.7 m. Figure 4-1 and Figure 4-2 show the realization of a birdcage coil loaded with the human model, and an unloaded high-pass birdcage resonator in the FDTD grid. Excitation ports are also illustrated.

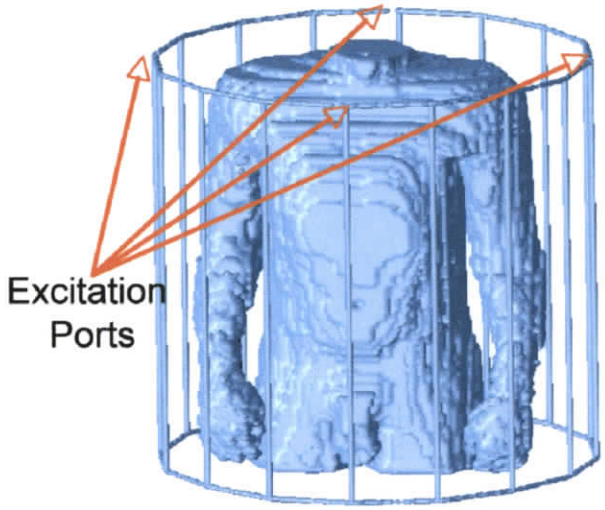

Figure 4-1: Schematic representation of a high-pass birdcage coil loaded with the human model within the FDTD (5 *mm*) grid.

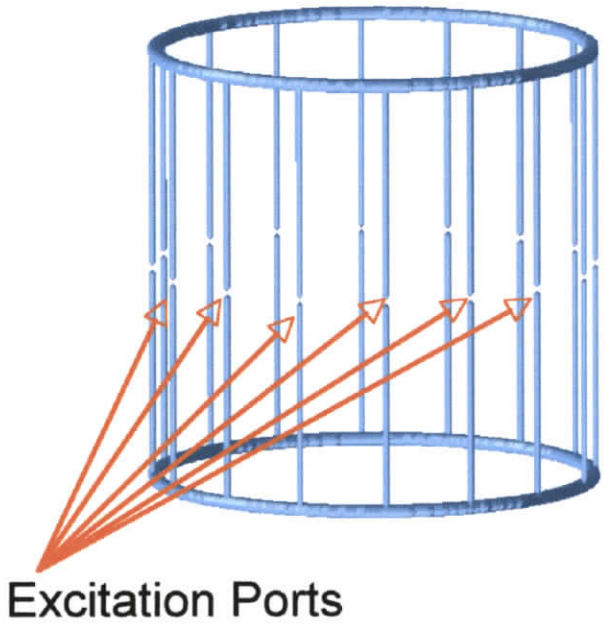

Figure 4-2: Schematic representation of an ideal birdcage coil within the FDTD (5 *mm*) grid.

In the resonant coil, a total of 16 lumped capacitors were placed at the mid-points between the rungs in both the upper and lower end-rings. By iteratively adjusting the values of capacitors [37] placed across all gaps in both the end-rings, a capacitance of 20 pF was chosen. A numerical representation of lumped capacitors was inserted into the FDTD grid in accordance with [38]. The capacitive lumped elements were positioned along the Cartesian axes, namely x or y.

For an x-directed lumped element located in the FDTD space at $E_x|_{i,j,k}$, the behavior of a capacitor is described by the following voltage-current characteristic:

$$I_x|_{i,j,k}^{n+1/2} = \frac{C\Delta x}{\Delta t}\left(E_x|_{i,j,k}^{n-1} - E_x|_{i,j,k}^{n}\right); \qquad J_L = \frac{I_x|_{i,j,k}^{n+1/2}}{\Delta y \Delta z}. \tag{4.1}$$

where J_L is the lumped electric current density, and I_x is the element current.

The integrity of the electromagnetic field calculation was ensured by choosing a Yee cell small enough – 5 ***mm*** for all models – to properly characterize the structure of the birdcage coil including the excitation source and the lumped capacitors.

The birdcage resonator was modelled with its length parrallel to the z-component of the FDTD space and the end-rings in the x-y plane. A stair-step approximation was used to model the curved section of the birdcage coil. Figure 4-3 and Figure 4-4 show the stair-step approximation of the end-ring of the ideal birdcage coil and the high-pass resonator. In the case of the high-pass resonator (Figure 4-4), the gaps in the end-rings represent the location of the lumped capacitors.

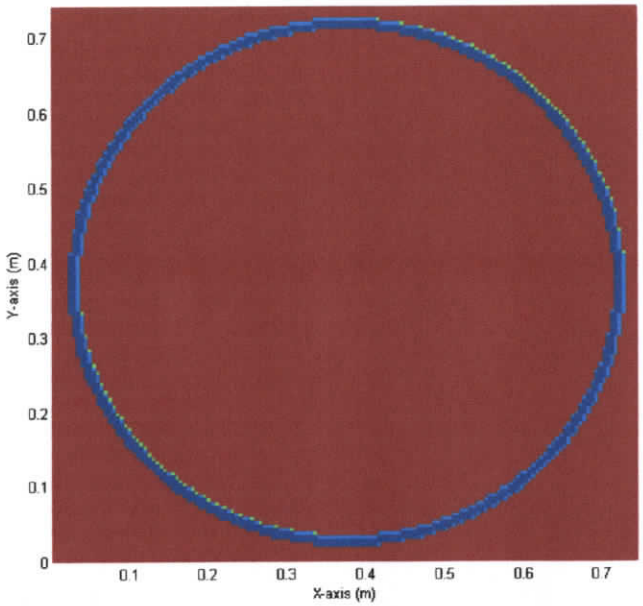

Figure 4-3: A stair-step approximation of the circular end-ring of the ideal birdcage coil

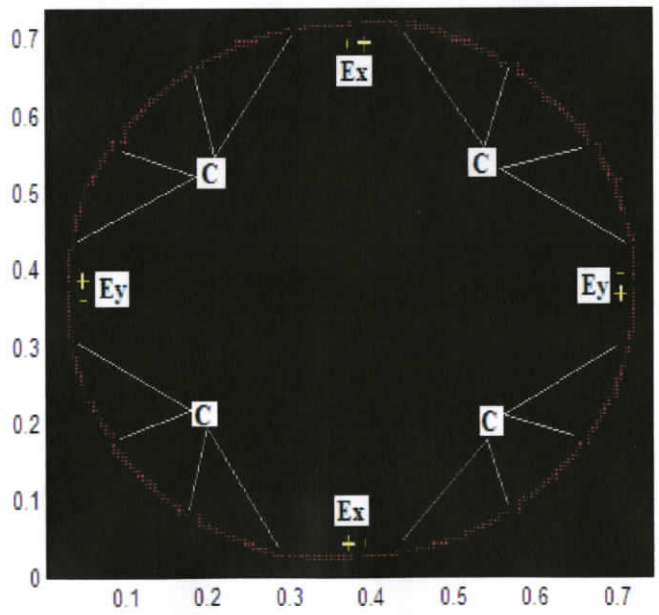

Figure 4-4: A stair-step approximation of the end-ring for the high-pass birdcage coil

The simulations were performed at 64 MHz using a frequency shifted Gaussian pulse to excite both coils. The source was a hard electric source implemented by assigning a time function representing the Gaussian pulse to specific components of the $\boldsymbol{E}$ field ($\boldsymbol{E_z}$ to excite the non-resonant coil, and $\boldsymbol{E_x}$ and $\boldsymbol{E_y}$ to excite the resonant coil) in the FDTD grid. An E_z sine-modulated Gaussian pulse at grid-point i_S is given by [38]:

$$E_z\big|_{i_S}^n = E_0 e^{-\left[(n-n_0)/n_{decay}\right]^2} - \sin\left[2\pi f_0 (n-n_0)\Delta t\right] \qquad (4.2)$$

where n_0 is the time-step where the time waveform is centered at, n_{decay} is the number of time-steps at which the pulse decays to zero, and f_0 is the central frequency of the carrier.

To get the spectrum of the pulse to be uniform over the range of interest the pulse width must be adjusted. A bandwidth of 30 MHz proved to be appropriate for these simulations.

In the case of the high-pass birdcage resoantor, a 4-port excitation was achieved by applying the same input to the E_x and E_y component of the electric field (Figure 4-4) with a progressive phase shift of $\pi/2$. The excitation ports were located on the upper end-ring of the birdcage coil with the separation between them being one quarter of the circle on the perimeter of the end-ring. The location of the excitation ports, their polarity and the position of the lumped capacitors is depicted in Figure 4-4.

The non-resonant coil – ideal birdcage coil with no capacitors – was excited at the midpoint of each of the 16 legs (Figure 4-2) with a progressive phase shift of 22.5 degrees. For both configurations, a uniform circularly polarized magnetic field was desired inside the coil.

4.2 Body Models

Body models provide the necessary information about the spatial distribution of the electrical properties of tissues to the FDTD field solver. Three different body models were employed: cylindrical phantoms, a heterogeneous human torso model, and a heterogeneous human torso model with a pacemaker. Cylindrical phantoms were used to demonstrate the validity of our simulations, and helped to explain the results obtained for the complex models. The torso model was used to further verify our modeling, to compare the results with the published data, and because of the paucity of these data to generate new useful data. Finally, enhanced SAR around the pacemaker and its lead was evaluated using the heterogeneous torso model with a pacemaker.

4.2.1 Cylindrical Models

Two dielectric cylinders of different size and composition were employed as simple human body models. The dimensions considered were: a large cylinder with a radius of 0.4 *m* and a height of 0.71 *m*, and a smaller cylinder with a radius of 0.3 *m* and a height of 0.71 *m*. For each size of the two models, different tissue compositions were used: a 100% muscle model and a layered model. The layered model was constructed using five concentric cylinders with different thicknesses and dielectric properties. Each layer represented a different tissue type with the core layer being muscle. The muscle core was covered by layers of fat, blood, bone, and skin, respectively. The cross section of the layered model is shown in Figure 4-5. The characteristics of these models are given in Table 4-1. The electrical properties of the tissues at 64 MHz are given in Table 4-2.

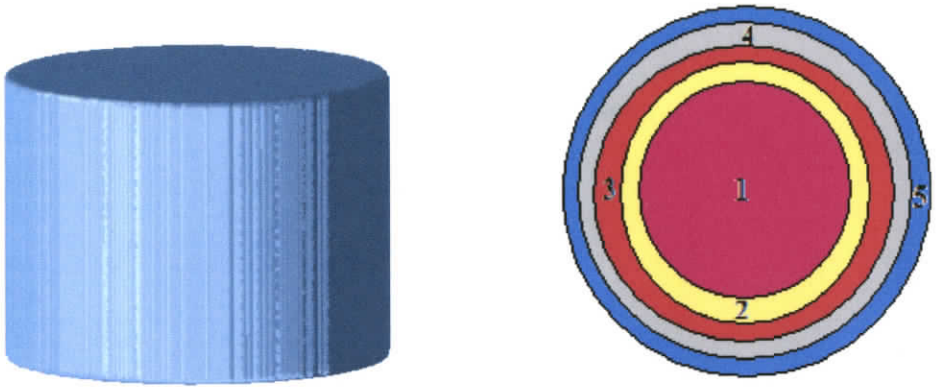

Figure 4-5: Illustration of a layered cylindrical phantom

Table 4-1: Dimensions of the layered models

	Region 1: MUSCLE radius (cm)	Region 2: FAT Thickness (cm)	Region 3: BLOOD Thickness (cm)	Region 4: BONE Thickness (cm)	Region 5: SKIN Thickness (cm)
Large Layered Cylinder	19.5	1.5	1.5	1.5	1.5
Small Layered Cylinder	16.0	1.0	1.0	1.0	1.0

4.2.2 Heterogeneous Torso Model

A high-resolution computer model of the human body is invaluable for biomedical research studies. An anatomically realistic human model previously developed at the University of Victoria was used in conjunction with the FDTD method to compute the electromagnetic fields induced inside the body. This model was based on MRI images taken at 3.6 mm separations from a male of an average height and weight. The MRI images were segmented into voxels in the shape of cubes. The model was then re-sampled to produce 5 mm resolution voxel model used in this work. The body model was composed of approximately 0.79 million cells and described by an array of integers of $112 \times 49 \times 144$. Overall, 30 distinct tissues were present. Electrical properties at 64 MHz were assigned to the tissues. Table 4-2 lists the characteristics of the tissues in the model at 64 MHz. Figure 4-6 gives views of the model surface and some selected organs and tissues.

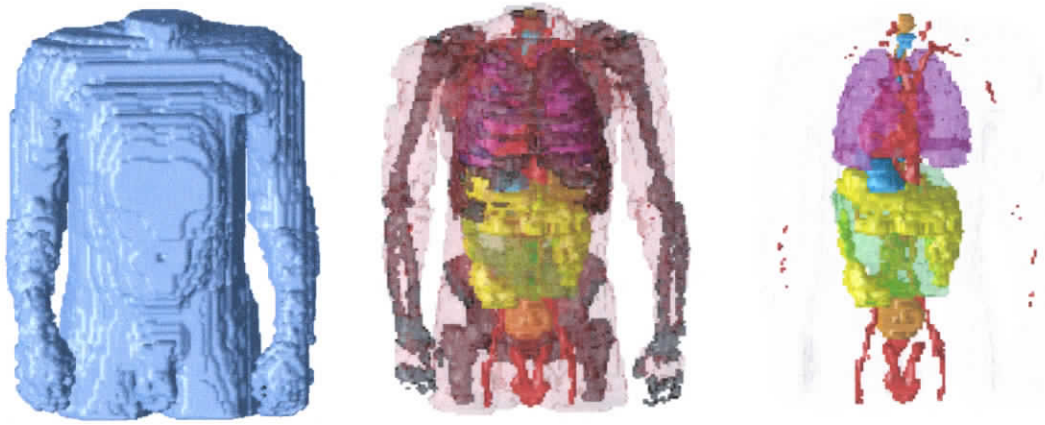

Figure 4-6: View of the torso model and selected organs and tissues

Table 4-2: Tissue Properties at 64 MHz for the Torso Model

Tissues	Dielectric Constant	Conductivity	Density
Air	1.00	0.000	0.00
Bladder	24.59	0.287	1.02
Blood	86.45	1.207	1.06
Bone	16.68	0.059	1.48
Bone marrow	16.43	0.154	1.08
Bowel	118.35	1.591	1.04
Gray Matter	97.42	0.511	1.04
Cartilage	62.91	0.452	1.20
Colon	94.65	0.638	1.02
CSF	97.31	2.066	1.01
Fat	13.64	0.066	0.92
Gall bladder	105.44	1.482	1.00
Heart	106.51	0.678	1.03
Kidney	118.56	0.741	1.03
Liver	80.56	0.448	1.06
Lung	37.10	0.289	0.26
Muscle	72.23	0.688	1.04
Prostate/testes	84.52	0.885	1.04
Skin	92.17	0.436	1.10
Spleen	110.56	0.744	1.04
Stomach	85.82	0.878	1.04
Thyroid	73.94	0.778	1.04

4.2.3 Torso Model with Pacemaker

A metallic box representing a pacemaker pulse generator was implanted in the fat tissues in the left side of the chest in accordance with clinical placements. A pacer lead was threaded through veins from the pacemaker generator and terminated in the ventricle of the heart. The lead was modeled two ways, as a perfect electric conductor (PEC) and an imperfect conductor, both with a cross section of 5 mm (equivalent to one FDTD cell) and a length of 371mm. For the imperfect conductor model, based on measurements of several models, a conductivity of 148.5 S/m was assigned to both the pacemaker and the

lead. Figure 4-7 depicts the location of the pacemaker generator and the wire threading into the ventricular pacing point.

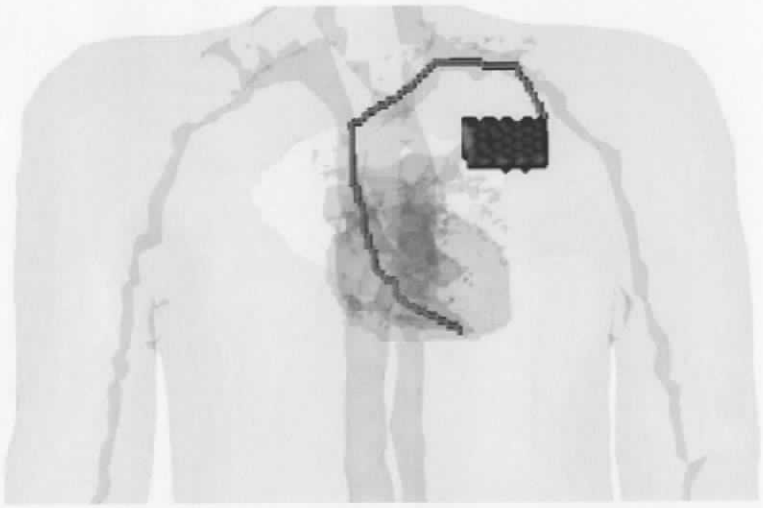

Figure 4-7: The pacemaker generator and the pacer wire

4.3 Computational Method

The finite-difference time-domain method (FDTD) – a widely used electromagnetic modeling technique – is based on the differential form of Maxwell's equations. The FDTD method, introduced in 1966 by Yee [39], is the most direct solution of Maxwell's equation:

$$\nabla \times \overline{H} = \overline{J} + \frac{\partial \overline{D}}{\partial t} \qquad (4.3)$$

$$\nabla \times \overline{E} = \overline{M} - \frac{\partial \overline{B}}{\partial t} \qquad (4.4)$$

where $\overline{E}$ and $\overline{H}$ are the electric and magnetic field strengths, $\overline{J}$ and $\overline{M}$ are the electric and magnetic current densities, and $\overline{D}$ are the $\overline{B}$ electric and magnetic flux densities.

Maxwell's differential equations are modified to central difference equations in such a way to derive the Yee algorithm. The equations are solved in a leap-frog manner – the electric field is solved at a given time step, the magnetic field is then solved at the next instant in time (Figure 4-8). A detailed description of the FDTD formulation is provided in [38] and [40].

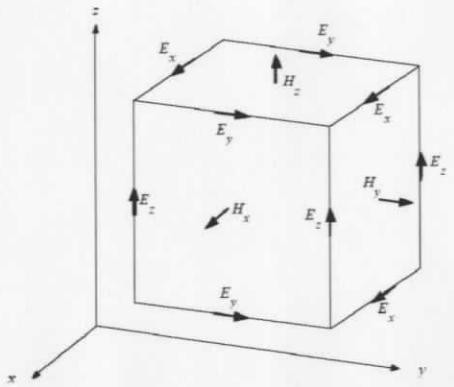

Figure 4-8: Yee Cell in FDTD method

The FDTD method is employed due to its flexibility and efficiency in solving complex heterogeneous geometry problems. Modeling of all materials such as dielectrics, magnetic materials, and biological tissues are possible using FDTD. The material properties at all points within the computational domain can be specified. Currently, the FDTD algorithm is the most widely adopted computational method for modeling the interactions of electromagnetic waves with biological tissues and SAR modeling.

To use the FDTD method, a computational domain where the simulation will be performed must be established. The FDTD formulation is based on a solution grid composed of rectangular boxes termed the Yee cell (Figure 4-8). Adequate accuracy of the results is achieved when the spatial increments in the Yee grid – Δx, Δy, and Δz – are

small enough (typically $\lambda/10$ - $\lambda/20$) compared to the shortest wavelength [38]. A Yee cell of 5 mm resolution matching the resolution of the torso model was chosen. The FDTD domain was chosen to have 148 cells in the x, y, and z directions – approximately 3.25 million cells – for a 5 *mm* spatial resolution model.

The computational domain is finite, and therefore a boundary must be established. An Absorbing Boundary Condition (ABC) is required to simulate the effect of an unbounded region. The Perfectly Matched Layer (PML), introduced by Berenger [41], is the most widely used abosorbing boundary condition because of its numerous advantages. This ABC is based on an artificial absorbing layer surrounding the simulation region that absorbs any outgoing wave. To account for the birdcage coil radiation, the perfectly matched layer with 6 layers was used. Reflections smaller than -60 dB for an arbitrary angle of incident can be achieved using the perfectly matched layer.

To ensure computational stability, the time step Δt was determined based on Courant Friedrichs stability criterion [42]:

$$\Delta t v_{\max} \leq \frac{1}{\sqrt{\frac{1}{\Delta x^2}+\frac{1}{\Delta y^2}+\frac{1}{\Delta z^2}}}, \qquad (4.5)$$

where $v_{\max}$ (m/s) is the maximum velocity of the propagating waves.

The time step Δt used was 9.6 *ps*. A sufficient number of iterations must be chosen such that the excitation signal has decayed significantly. This ensures the frequency domain data are not affected by the late time signal. The simulations were performed for 16,000 iterations for the non-resonant coil and 100,000 for the resonant coil and ran for 33 and 371 hours, respectively, on the University of Victoria's Minerva Computing system.

5 Calculations of the Magnetic Flux Density

In the previous chapter, the birdcage and body models, and computational method were introduced. In this chapter the performance of the birdcage coils with various loadings at 64 MHz is analyzed. The results of several studies performed with the FDTD method and the body models are presented. Using these results the reliability of our simulation and methodology are assessed.

5.1 Currents in the Rungs of Birdcage Coil

Using full wave analysis the current distribution in the rungs of the birdcage coil was examined. In Chapter 2, the sinusoidal current distribution in the rungs was represented by equation *(2.9)*, namely:

$$I_i = I_{\max} \cos\frac{(i-1)\pi}{N}, \qquad (5.1)$$

where I_i is the current in the ith element, I_{max} is the maximum current, and N is the number of elements. Vaughan et al. [43] suggested that this current distribution was similar to that for a half wavelength dipole.

Figure 5-1 shows the plot of the current distribution in the coil element (rung) at 64 MHz for an unloaded coil, a coil loaded with the torso model, and a coil loaded with the cylinderical model. Data have been obtained by noting the current in the first element at the instant its polarity changes and measuring the current in the subsequent rungs at the same instance of time. Examining the plot indicates that for a loaded coil, the interaction between the coil and the load induces additional currents in the rungs of the coil. The

torso model is larger and thus closer to the coil, it hence exhibites a stronger interaction than the cylinderical model. This leads to greater induced currents in the coil. These results are in agreement with data presented in [37].

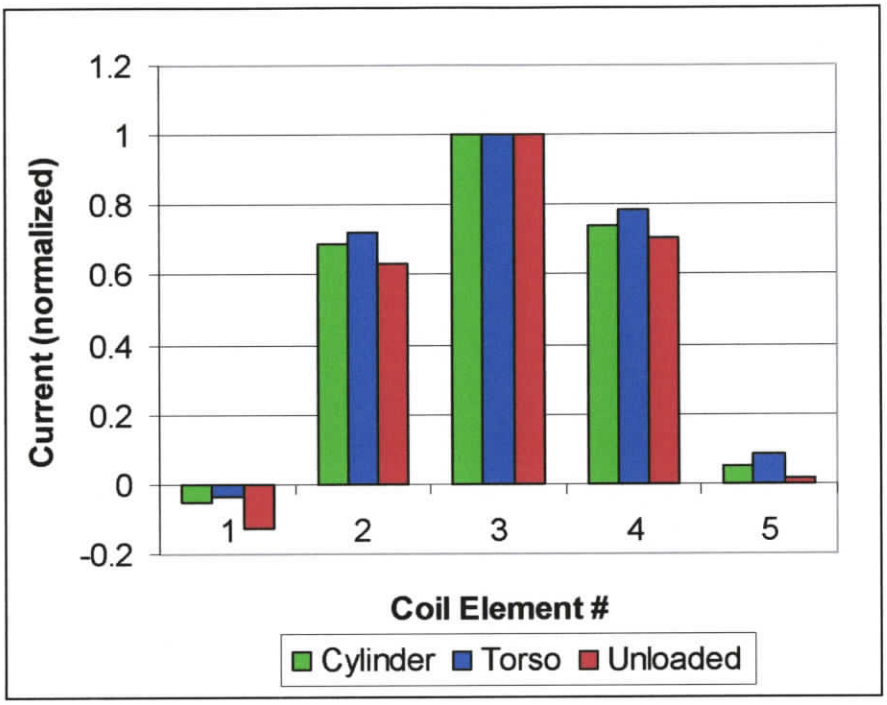

Figure 5-1: The current distribution on the coil rungs at 64 MHz

5.2 Axial Ratio

Circularly polarized magnetic fields provide the most effective way to couple energy into and out of the nuclei. A perfect circularly polarized magnetic field has an axial ratio of 1. The birdcage coils were therefore driven in such a way to produce circularly polarized fields. The non-resonant coil was excited at the midpoint of each of the 16 rungs with a progressive phase shift of 22.5°. The resonant coil was driven at four ports in the upper end-ring 90° apart in space with their phases set to 0, 90, 180, and 270 degrees, respectively.

The number of time steps in the FDTD simulations was chosen such that the signal had decayed significantly, thus, ensuring the frequency domain data were not affected by the late time signal (Figure 5-2). It should be noted from Figure 5-2 (e) and Figure 5-2 (f) that due to losses, the signal decayed much faster in the loaded resonant coil than in an unloaded one.

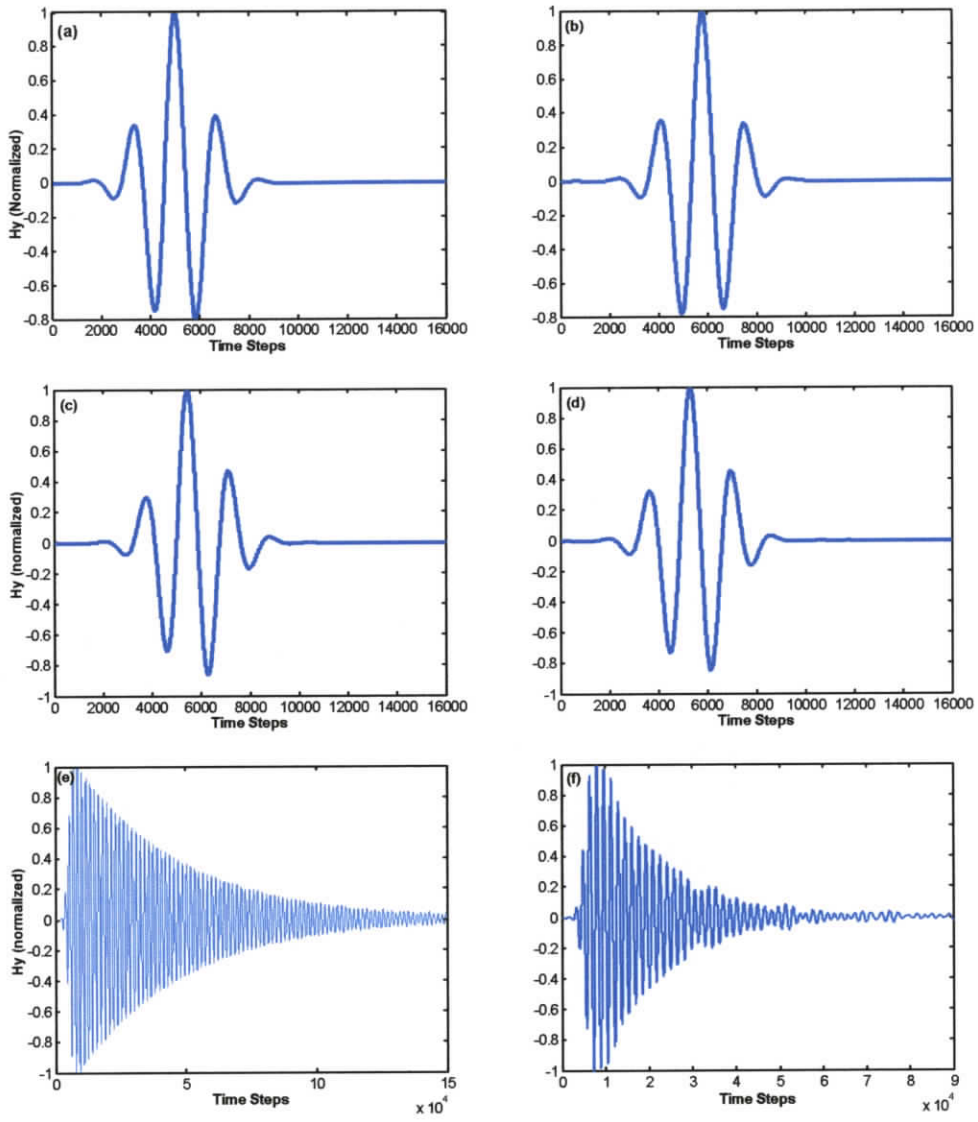

Figure 5-2: Time domain response inside the birdcage for (a) a non-resonant unloaded coil, (b) the non-resonant coil loaded with the cylindrical phantom, (c) the non-resonant loaded with the torso model, (d) the non-resonant coil loaded with the torso model and a pacemaker, (e) the resonant unloaded coil, and (f) the resonant coil loaded with the torso model.

Exciting the coil in this manner, gave a B_1 field that is highly uniform over the central region of the coil. Furthermore, due to the dependency of local SAR values on field polarization, using circularly polarized fields reduces SAR values [44].

Figure 5-3 and Figure 5-4 illustrate the axial ratio for both the resonant and non-resonant coils. It can be seen that circularly polarized fields are produced inside the resonant and non-resonant unloaded coils and coil loaded with the cylinder. The human torso model is larger than the cylindrical model and hence closer to the edges of the coil. This causes a strong coupling that disrupts the field symmetry. As well, the torso model, unlike the cylindrical phantom, lacks a circular symmetry, resulting in the induced currents to become more distorted. It can, therefore, be deduced that at 64 MHz, perfectly circularly polarized fields inside a birdcage coil are only generated when the model (object to be imaged) has a circular symmetry and is small relative to the size of the coil.

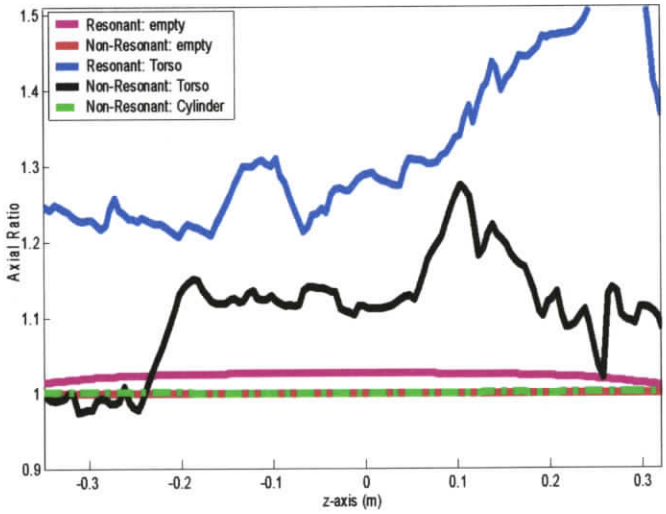

Figure 5-3: Axial ratio along the length of the birdcage for the resonant and non-resonant birdcage coil for different loadings.

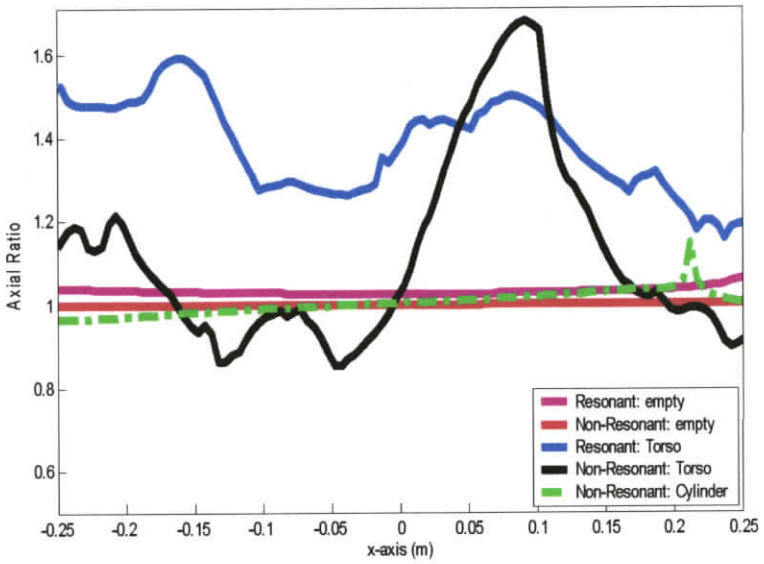

Figure 5-4: Axial ratio in the *x-y* plane of the birdcage for the resonant and non-resonant birdcage coil for different loadings.

5.3 Frequency Response of the Birdcage Coil

The frequency response of the coil has been obtained by applying the Fourier transform to the FDTD solution for the magnetic field. Since the frequency response at any point within the coil does not significantly differ with the location, the observation point has been arbitrarily chosen to be the centre of the coil.

For the resonant coil, its operation at the Larmor frequency is achieved by lumped capacitors. The lumped capacitors have been tuned using an iterative approach [37]. An initial guess is based on the capacitor values reported in the literature. The value of the capacitors has been iteratively adjusted until the desired resonance frequency has been achieved. Figure 5-5 displays the frequency response of the non-resonant and resonant coils at 64 MHz. The magnetic field data is used to determine the $\boldsymbol{B_1}$ field distribution

within the resonator. The frequency response with a frequency step of 1 MHz is presented.

The frequency spectrum of the non-resonant coil is centered at 60 MHz for all loadings. Since there is no additional loading, the coil inductance and capacitance determine the frequency response. However, when the high-pass birdcage coil is employed the coil is tuned with 20pF lumped capacitors (a total of 32, 16 in each circular ring) to 64 MHz (Figure 5-5). The resonant coil also has a significantly narrower bandwidth compared to that of the non-resonant coil.

Loading the non-resonant coil with the cylindrical model and the Torso model causes a negligible shift in the spectrum of the magnetic field at 64 MHz. This shift is even less apparent, practically non-existent for the resonant coil. This is not a surprising result, and similar data are reported by Ibrahim et al. [37].

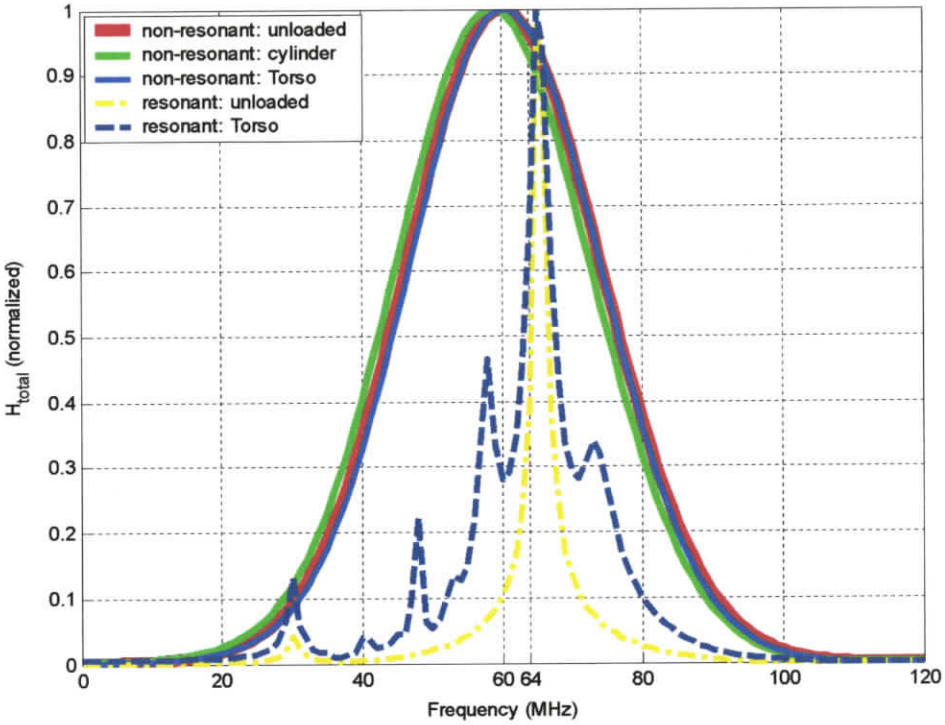

Figure 5-5: Frequency response of the magnetic field inside the coils for different loadings.

5.4 Spatial Uniformity

As previously mentioned, to obtain high quality MRI images, a uniform $\boldsymbol{B_1}$ field (the magnetic field of the RF pulse generated by RF coils is called the $\boldsymbol{B_1}$ field) must be produced in the volume of interest. Failure to produce a spatially uniform $\boldsymbol{B_1}$ field causes some of the nuclei not to be excited, or excited with different flip angles, leading to poor image contrast and signal to noise ratio (SNR).

The magnetic field uniformity of the non-resonant and resonant coils was investigated for different loadings: an unloaded coil, a coil loaded with the cylindrical models, and loaded with the torso models.

The circularly polarized magnetic field inside the birdcage coils for different loadings is displayed in Figure 5-6 to Figure 5-9. The maximum $\boldsymbol{B_1}$ field values in Figure 5-6 and Figure 5-8 correspond to zero on a logarithmic scale. In the plots in Figure 5-7 and Figure 5-9, the magnetic field is normalized to the value in the center of an unloaded coil. The magnetic field strength measured at the center of the coils is given in Table 5-1. The resonant coil is excited in four ports in the upper end-ring, while the non-resonant coil is excited at the midpoint of each rung.

Figure 5-6 shows the $\boldsymbol{B_1}$ field for axial slices inside the non-resonant coil excited at 16 ports. The $\boldsymbol{B_1}$ field distribution remains homogeneous for the coil loaded with the cylindrical model. Figure 5-7 displays the total $\boldsymbol{B_1}$-field along the x- and z- axis at the center of the coil: the fields are very homogeneous in the central regions of the coil for the unloaded coil and the coil loaded with the cylinder. The total magnetic field is 98% homogeneous (the difference between the maximum and minimum value of the H_{total}-field is 2% or less) for the unloaded non-resonant coil, and 81% for the coil loaded with the cylinder. Deterioration in the uniformity of the magnetic field is apparent for the loaded coils, particularly at the boundaries of the models. The fields are further distorted near the edges of the coil.

The coils loaded with the torso models (with and without pacemaker) exhibit a reduction in field homogeneity (Figure 5-6 and Figure 5-7). The reduced homogeneity can be attributed to several factors. The torso model is larger than the cylindrical model and therefore closer to the elements of the coil. This introduces strong coupling that distorts the fields inside the coil. As well, the attenuation of the fields by the lossy tissue, and the additional magnetic field created inside the body due to eddy currents induced inside the body contribute to the field inhomogeneity.

Figure 5-8 and Figure 5-9 show the field distributions in the resonant coil excited in four-ports in the upper end-ring. Comparing the results with the non-resonant coil, a less homogeneous magnetic field is noted for the unloaded coil. The field homogeneity is reduced to 94% of the imaging volume (along the *x*-axis). The higher field homogeneity in the non-resonant coil is a direct result of the progressive phase shift of 22.5 degrees in 16 rungs rather than 4 point excitation with the corresponding phase shift of 90 degrees. The examination of Figure 5-7 and Figure 5-9 indicates a better overall homogeneity along the *x*-axis when the resonant coil is loaded with the torso models.

Table 5-1: Magnetic field strength (A/m) at the center of the coil

	Unloaded	**Torso**	**Torso with pacemaker**	**Cylinder**
Resonant	0.80	0.56	0.56	-
Non-resonant	0.079	0.089	0.089	0.049

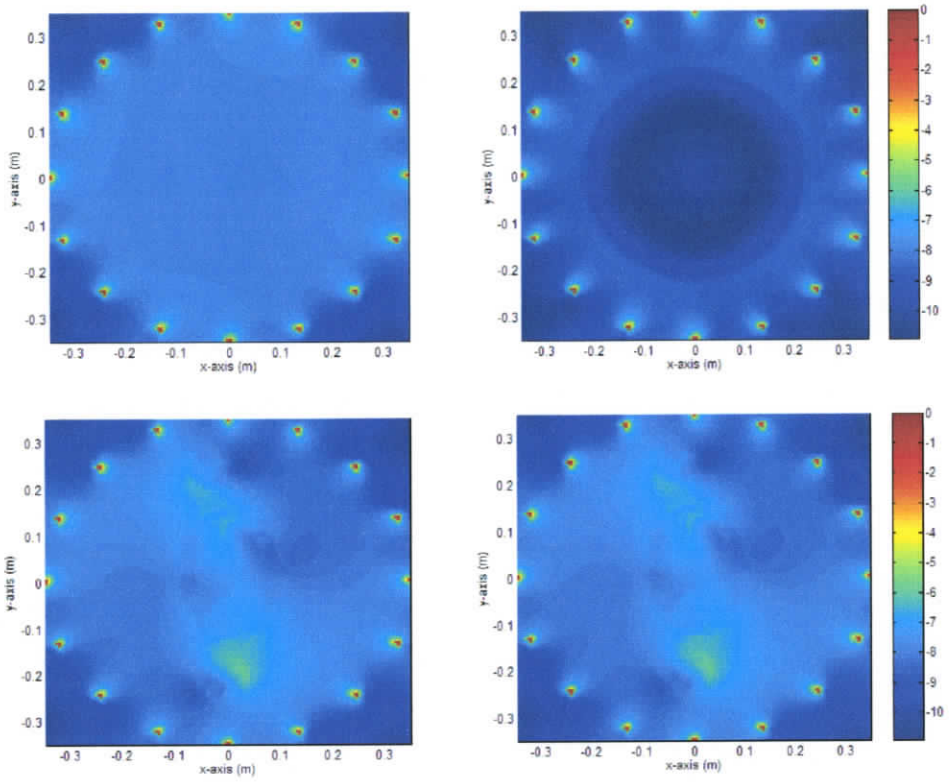

Figure 5-6: The B_1-field at 64 MHz at the centre of the non-resonant coil: (top-left) unloaded coil, (top-right) muscle cylinder, (bottom-left) torso, and (bottom-right) torso with pacemaker.

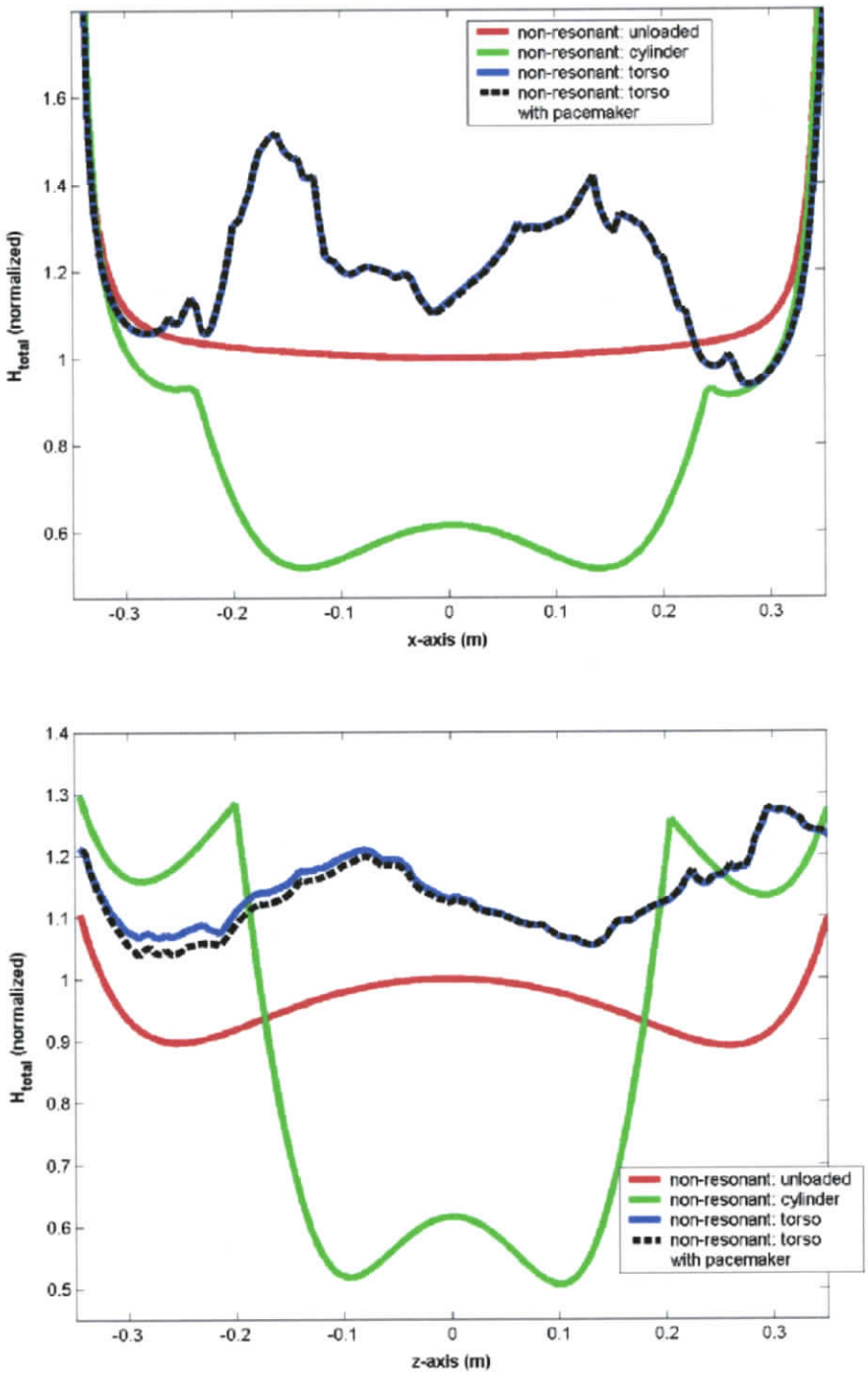

Figure 5-7: Total magnetic field in a non-resonant birdcage coil along the central plane as a function of x (top), and z (bottom). All values are normalized to the value at the center of an unloaded non-resonant coil.

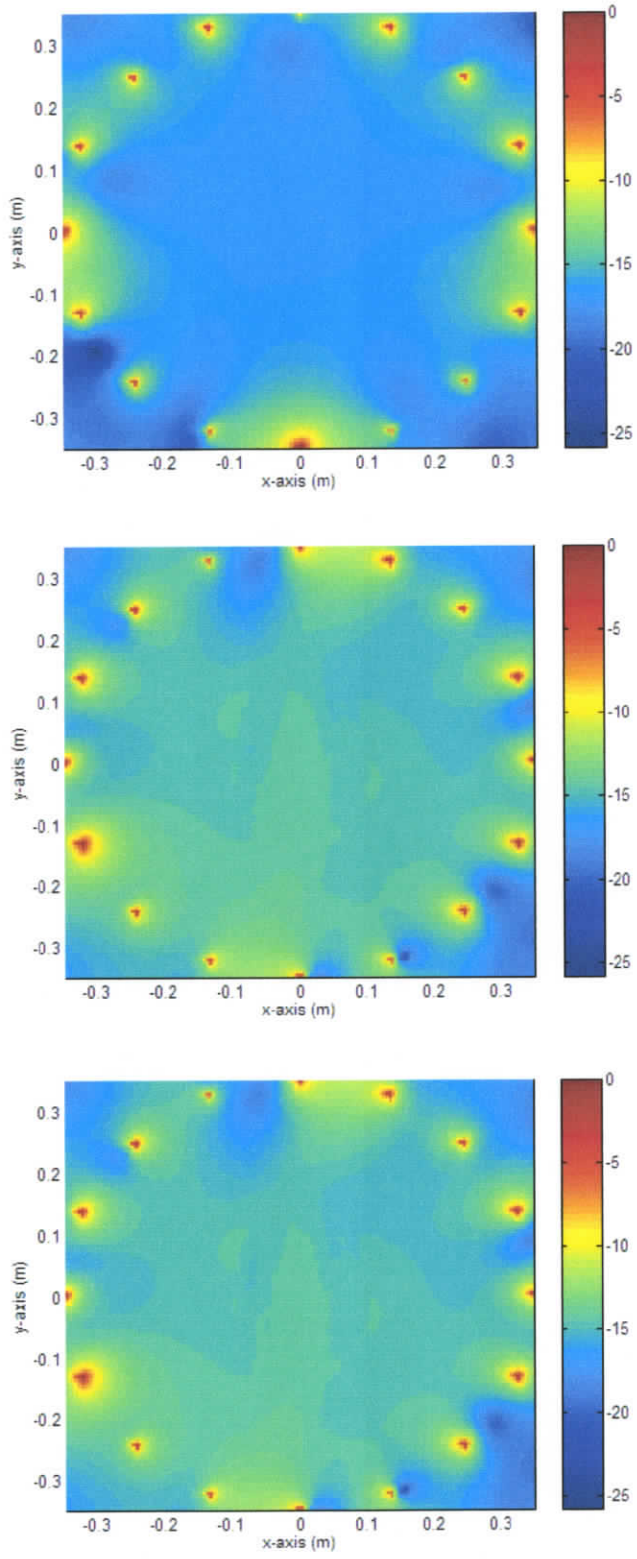

Figure 5-8: The B_1-field at 64 MHz at the centre of the resonant coil: (top) unloaded, (middle) loaded with torso, (bottom) loaded with torso with pacemaker

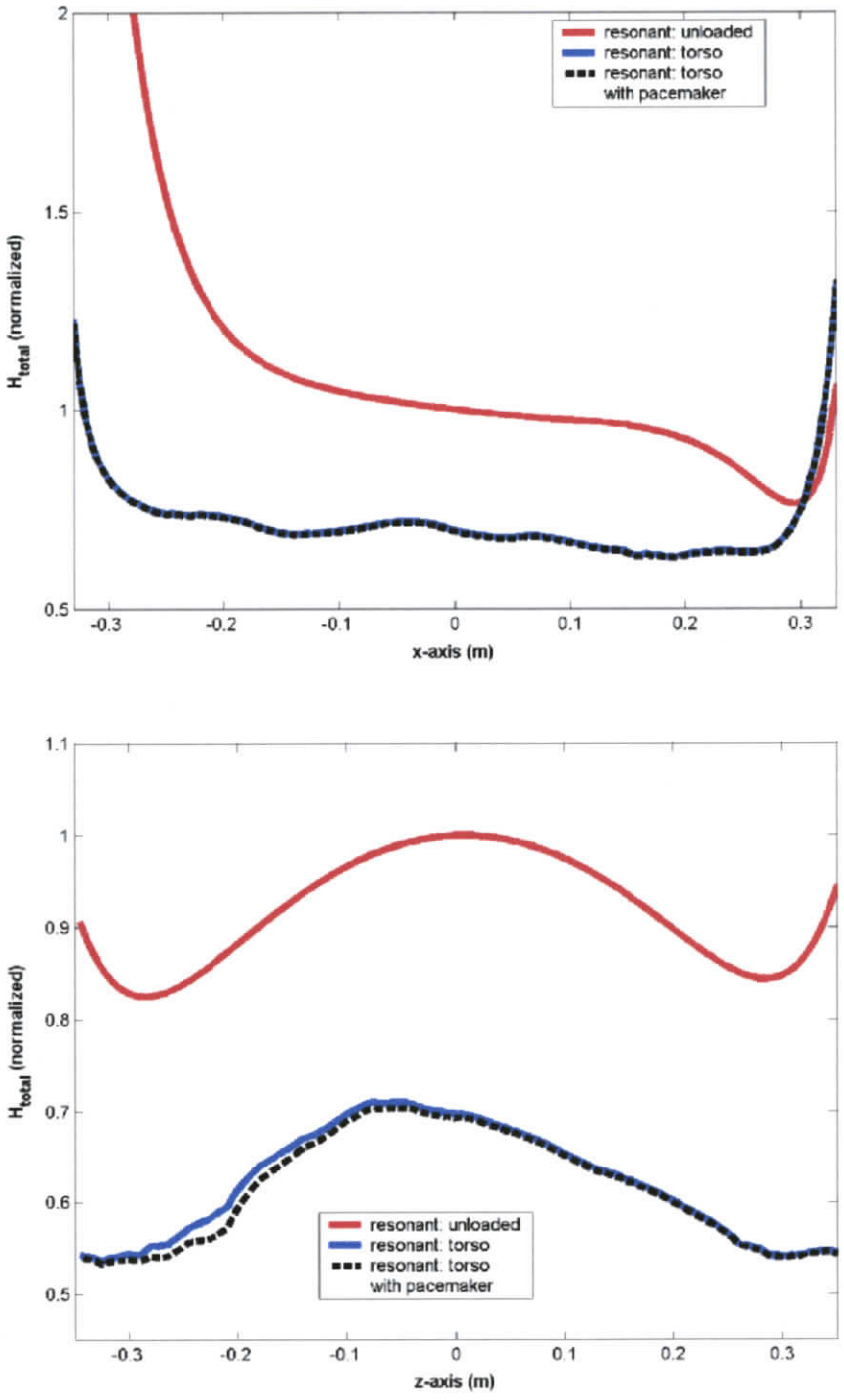

Figure 5-9: Total magnetic field in the resonant coil along the central plane as a function of x (top), and z (bottom). All values are normalized to the value at the center of an unloaded resonant coil.

5.5 Summary

The performance of the birdcage coil for various loadings was investigated at 64 MHz. Nearly perfectly circularly polarized magnetic fields (with an axial ratio close to one) were achieved in the unloaded coil and the coil loaded with cylindrical models for 16- and 4-port excitation. The torso model – unlike the cylindrical model – was heterogeneous and lacked a circular symmetry and, as expected, this resulted in deterioration of circular polarization. The field uniformity was observed for resonant and non-resonant unloaded coils. A reduction in the uniformity was observed for the coil loaded with the cylindrical and the torso models. This was attributed to the interaction of the fields with the models. These findings are in agreement with those reported in the literature.

The magnitude of the magnetic field at the center of the coils was evaluated with the same excitation current. A much stronger field was observed at the center of the resonant coil for all loadings. This finding is also in agreement with data in the literature.

6 Specific Absorption Rate

A part of the RF energy transmitted by the coil is absorbed by the body during MRI procedures. An increase in temperature results in the tissues due to the absorbed RF energy. This elevation of temperature in the tissues could lead to overheating or even burning and therefore safety concerns. The RF power deposited in tissues is measured by the means of specific absorption rate (SAR), as defined in section 2.3.

This chapter presents results from the studies undertaken in this thesis pertaining to RF power deposition in the body during MRI procedures. While the focus is on a realistic model of the human body with and without the implanted pacemaker model, data are also given for the cylindrical models for the purpose of rationalization and interpretation of the results obtained for the complex models.

6.1 Cylindrical Models

SAR calculations are performed for the cylindrical models to verify our modeling. The properties of these models are described in Chapter 4. Two different size cylinders with different compositions are used to represent a simple human body model. The simple structure of the models provides the opportunity to study the interactions of the fields from the source with the object of interest.

Figure 6-1 illustrates the axial views of the 1g SAR maps at the center of the non-resonant coil for a homogeneous cylindrical muscle model and a layered cylindrical model. The multilayer cylindrical model consists of different biological tissues, namely, muscle, fat, blood, bone, and skin. In the muscle cylinder (diameter = 48 cm) higher

SAR occurs close to the surface, while in the smaller diameter cylinder the center has the greatest SAR (Figure 6-1). The RF fields are attenuated in tissue as a function of depth, thus weaker fields in the center of the large cylinder. A different interaction is observed when the coil is loaded with the small cylindrical model (diameter = 40 cm). In this case, the RF radiation penetrates deeper in the small model resulting in high SAR values. Similar results are observed in the layered models (Figure 6-1). The SAR distribution is however affected by the different electrical properties of the tissues and reflections at the tissue boundaries. In general, when dealing with large models, areas of the high SAR occur at the periphery of the body. Additionally, the proximity to the edges of the coil increases the SAR levels. For the smaller models the peak SAR is inside the model. These findings are consistent with published studies [5].

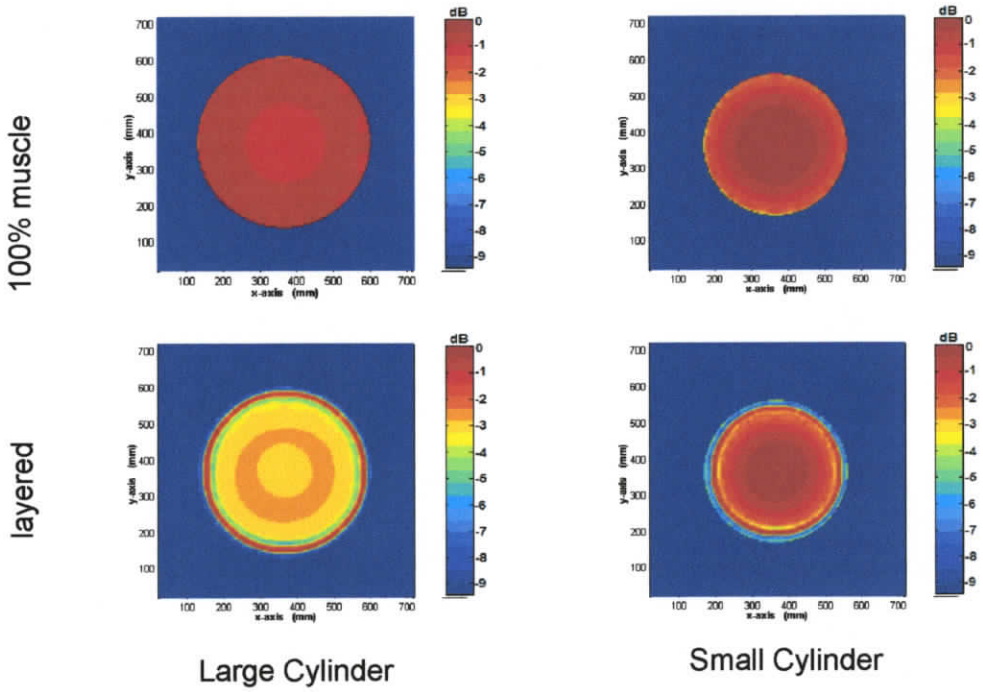

Figure 6-1: 1 gram SAR distributions at 64 MHz for homogeneous and layered muscle cylindrical models (d = 48 cm for the large cylinder and d = 40 cm for the small cylinder).

To obtain additional information helpful in explaining the results of the simulations of the pacemaker in the complex body model, thin metallic rods representing leads with lengths of 10 cm and 20 cm and a radius of 5 mm (equivalent to one FDTD cell) are placed in the central plane of the large homogeneous cylindrical model, as shown in Figure 6-2.

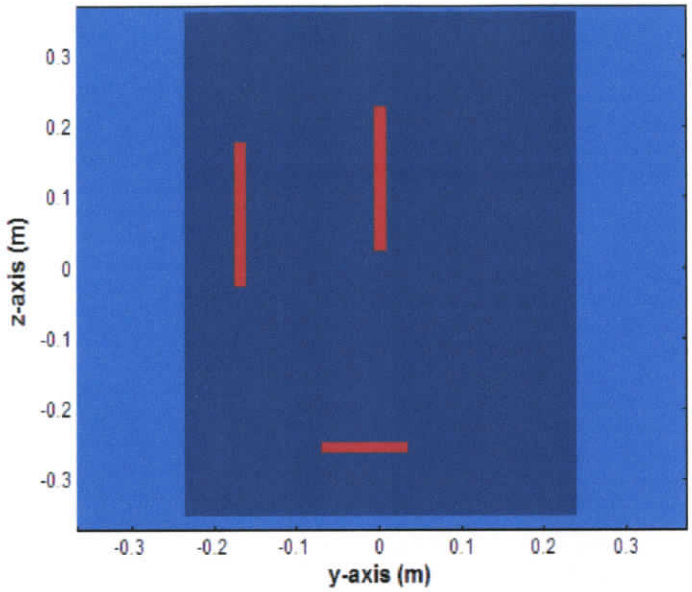

Figure 6-2: Location of metallic rods in a large homogeneous cylindrical model

Figure 6-3 illustrates SAR distribution in the cylinder with and without thin metallic rods in the non-resonant birdcage coil. High SAR values are confined to the ends and surface in the periphery of the cylinder with no metallic rods. The cylindrical model is longer than the coil surrounding it. This explains the SAR levels in the portion of the cylinder lying in the plane of the end-rings. These high SAR values are an artifact due to the length of the cylinder and the high electric field strengths in the end-rings. Metallic rods perturb the SAR distribution in the cylinder. Elevated SAR levels occur at the tips of the metallic rods situated in the high SAR regions near the surface of the cylinder (Figure 6-3). A maximum 1g SAR value of 2.53 W/kg is computed at the tip. The weak fields at

the center of the cylinder lead to minimal interactions with the rod. As apparent from Figure 6-3, no SAR enhancement due to the presence of the rod is detected in the core –a region of low SAR– of the cylinder.

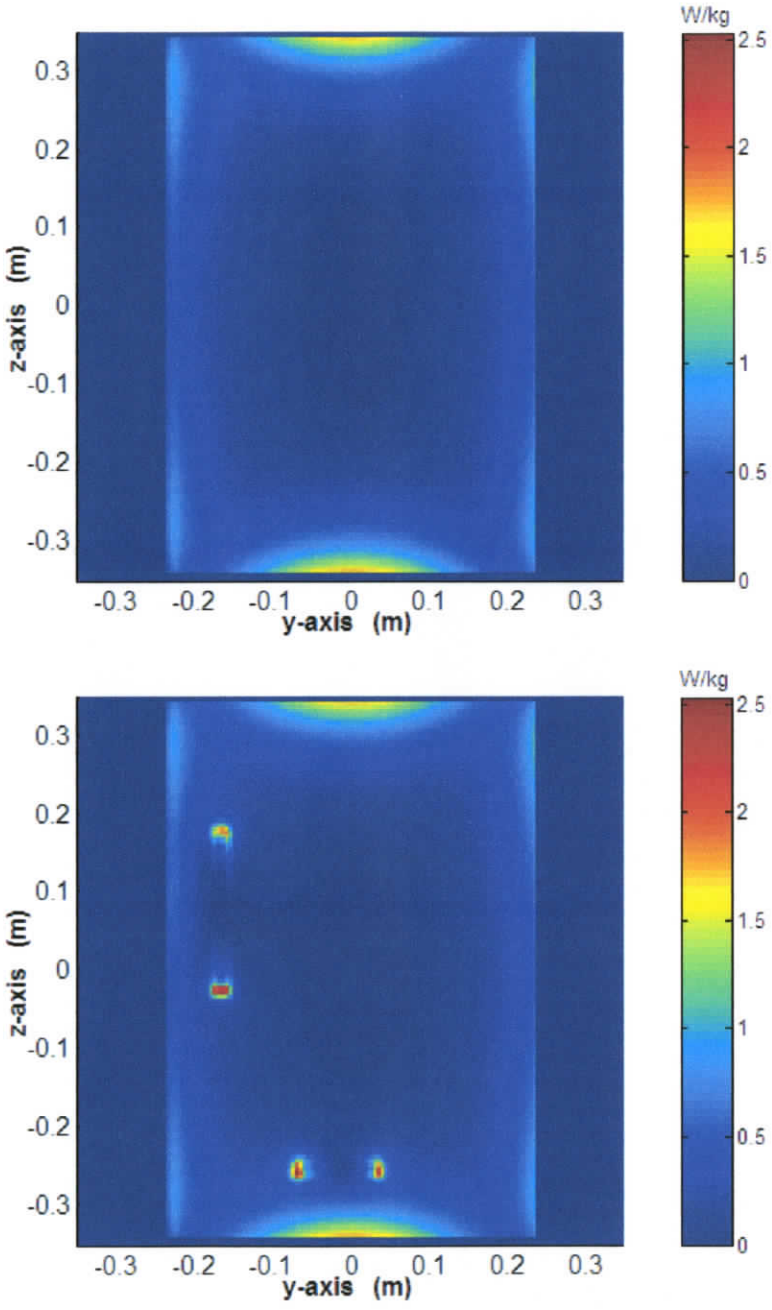

Figure 6-3: Distribution of 1g SAR (W/kg) in the large homogeneous cylinder without metallic rods (top) and with metallic rods (bottom).

6.2 Torso Model

The following calculations are presented for a human torso model in a non-resonant birdcage coil at 64 MHz. One would anticipate that the coupling between the coil and the body model would considerably affect the SAR values near the edges of the coil. This is demonstrated in the following figures. Figure 6-4 shows a sagittal and an axial slice of the SAR inside the human torso model (the sagittal cross-section is in the center of the body, and the axial cross-section is across the upper chest). Additional cross sections of the SAR inside the human body model are given in Figure 6-5 and Figure 6-6. Similarly to the cylindrical model, the high SAR values are observed in the periphery of the body. This is where the interactions between the coil and body model are the strongest. High SAR values are as well detected in some internal tissues with high conductivity.

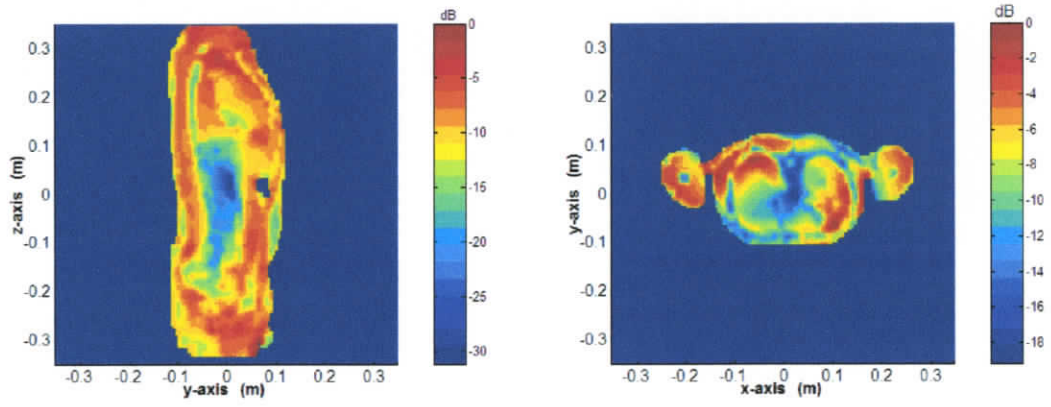

Figure 6-4: 1g SAR distribution inside the torso model at 64 MHz for a non-resonant coil; data normalized to the maximum value (0 dB)

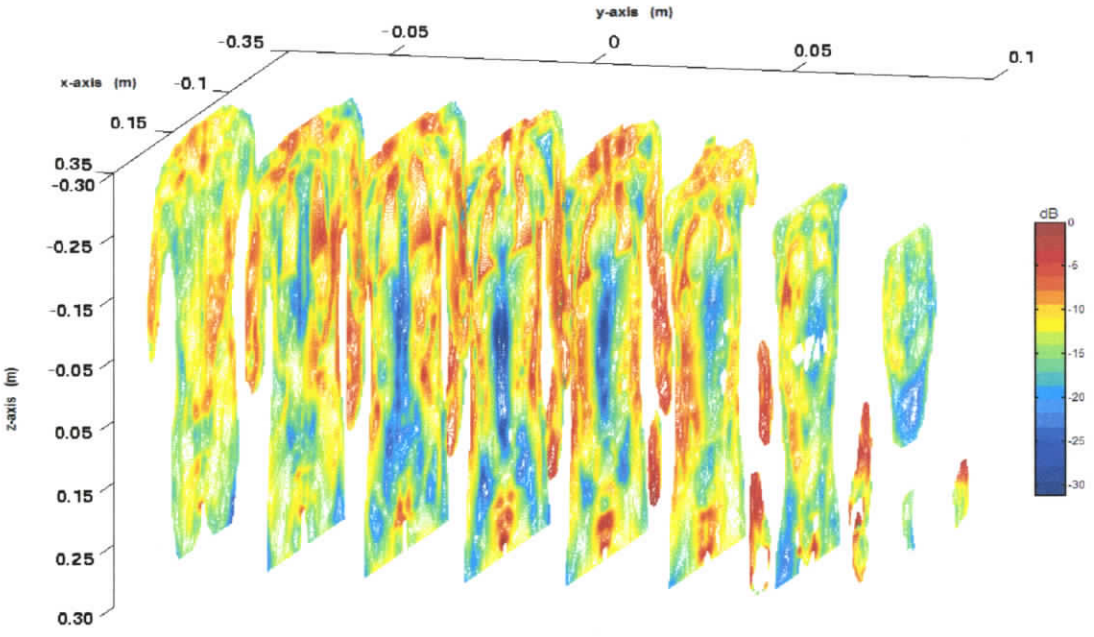

Figure 6-5: Coronal slices of 1g SAR distribution in the torso model for the non-resonant coil

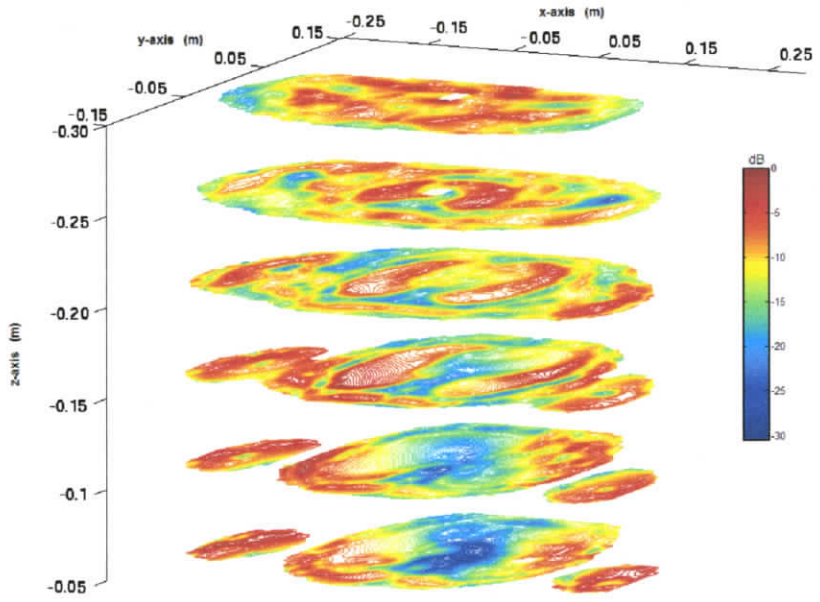

Figure 6-6: Axial slices of 1g SAR distribution in the torso model for the non-resonant coil

The amount of absorbed energy, and therefore SAR, is dependent on the tissue characteristics such as dielectric properties, size, shape, and orientation [31]. The hands are small-scale tissue features and are closest to the edges and the excitation ports of the coil. Hence, significant interactions with the coil exist here. For this reason, the highest overall 1g SAR value is observed in the hands. Local hot spots are also observed in the neck and hip region of the model close to the end-rings where the electric field strengths are high. As it was observed with the cylindrical models, this is an artifact due to the model's terminations lying in the plane of the end-rings.

Distribution of the maximum 1g SAR in two orthogonal planes through the torso model is given in Figure 6-7 for the non-resonant coil. A maximum 1g SAR of 16.9 W/kg is computed in the periphery (hand) of the body. A whole-body average SAR of 0.63 W/kg is calculated. In other studies, [5] and [30], the maximum 1g SAR has also been associated with tissues in the periphery of the body. Table 6-1 lists the maximum 1g SAR from this investigation and those of others. It should be noted that only the results of [30] can be directly compared to the result computed in this study.

Table 6-1: Maximum 1g SAR

	Computed Results	Results from [30]	Results from [5]
Normalization	1.957 μT	1.957 μT	1 W/kg
1g SAR_{max} (W/kg) (non-resonant)	16.9	15.2	16.5
1g SAR_{max} (W/kg) (resonant)	1.28	-	-

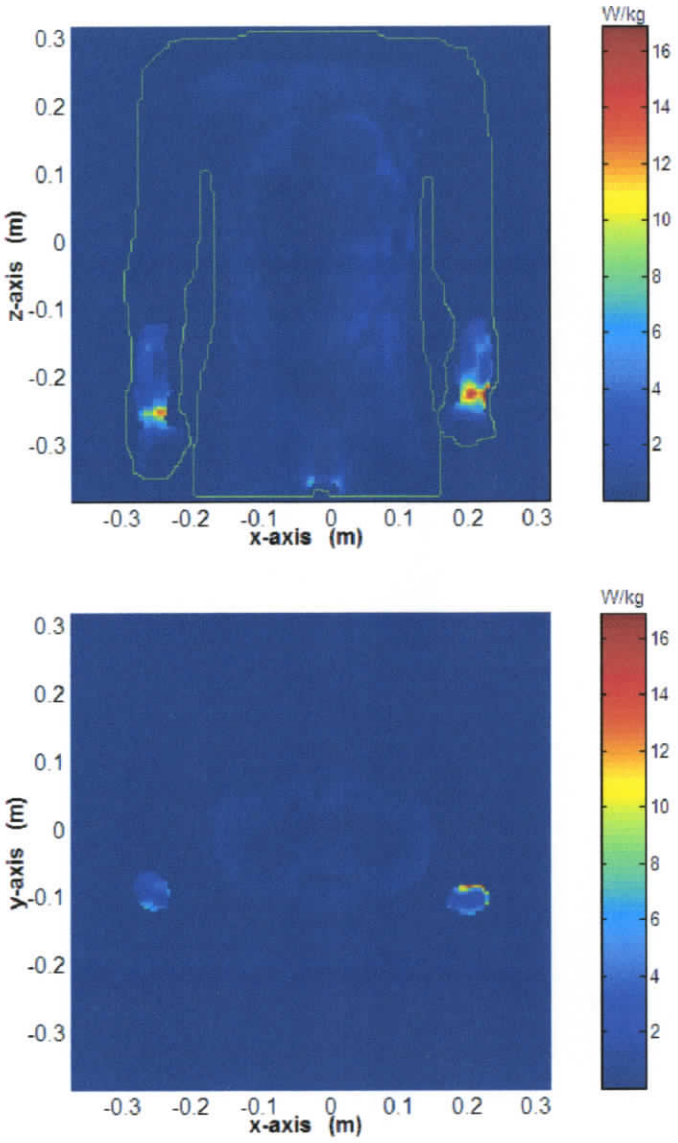

Figure 6-7: Maximum SAR distribution in the torso model for the non-resonant coil at 64 MHz.

Figure 6-8 shows the sagittal and the axial views of the SAR inside the human torso model in the resonant coil. Additional slices of the SAR distribution in the torso model are illustrated in Figure 6-9 and Figure 6-10. Similarly to the non-resonant coil, high SAR values occur in the periphery of the body. However, a different SAR pattern is observed in the resonant coil; contrary to the results from the non-resonant coil, elevated

SAR levels are mainly associated with the tissues in the front and back of the body at the center of the coil. This most likely can be attributed to the peculiar field distribution in the resonant coil. In the resonant coil configuration used in this study, excitation ports and reactive elements are situated in the end-rings. As shown in Chapter 5, this configuration results in a different magnetic field distribution than that in the non-resonant coil. The magnetic field in the resonant coil (Figure 5-9) is uniform along the *x*- and *y*- plane; however, it becomes stronger along the *z*-plane at the center of the coil. This causes the induced SAR to be greater in this region.

Figure 6-11 illustrates the maximum 1g SAR distribution in the torso model for the resonant coil. The maximum SAR value is in the front part of the body in the right pectoral cavity, consistent with the high SAR regions. A maximum 1g SAR of 1.25 W/kg is in the lungs and 1.02 W/kg in the pectoral muscle.

In general, lower SAR levels are observed in the resonant coil for the same magnetic field in the empty coil. This phenomenon can be described through the quality factor (*Q*-factor) of the RF coils. The quality factor is a measure of the loss of a resonant circuit. For a complex circuit such as the birdcage coil the quality factor can be conveniently obtained as [10]

$$Q = \frac{\omega_r}{\Delta\omega} \qquad (6.1)$$

where ω_r is the resonant frequency and $\Delta\omega$ denotes the bandwidth.

Generally, a circuit with a high *Q*-factor is desired as it implies low loss and low power dissipation. As mentioned earlier in Chapter 5, the resonant birdcage coil has a narrower

bandwidth than the non-resonant coil (Figure 5-5). From the relation in equation *(6.1)* it is evident that the resonant coil quality factor is higher than that of the non-resonant coil. The absorbed power and subsequently SAR are proportional to the power lost inside the resonator. Thus, the resonant coil with a high Q-factor minimizes the power dissipation and consequently results in reduced SAR levels in the tissues.

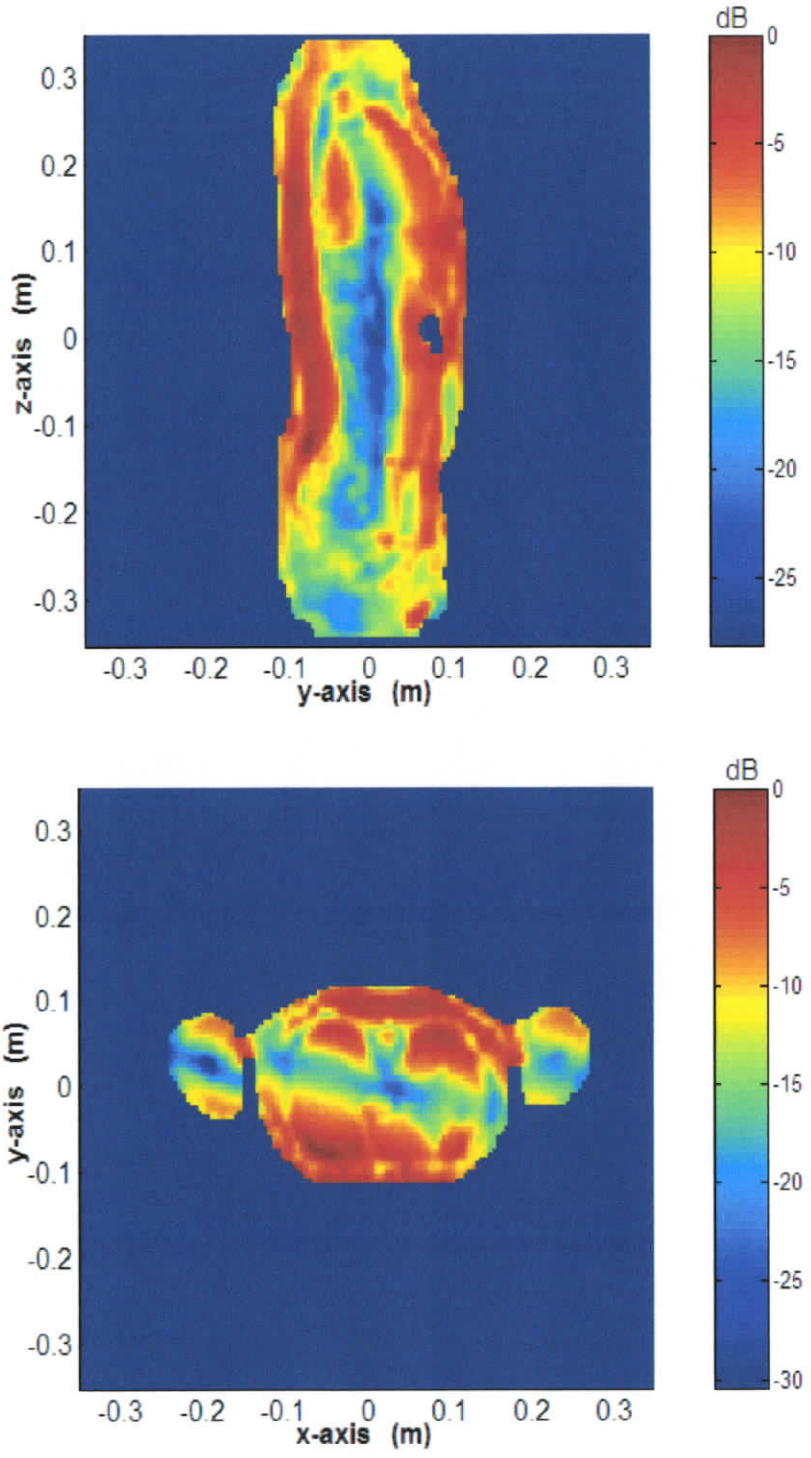

Figure 6-8: 1g SAR distribution inside the torso model at 64 MHz in a resonant coil.

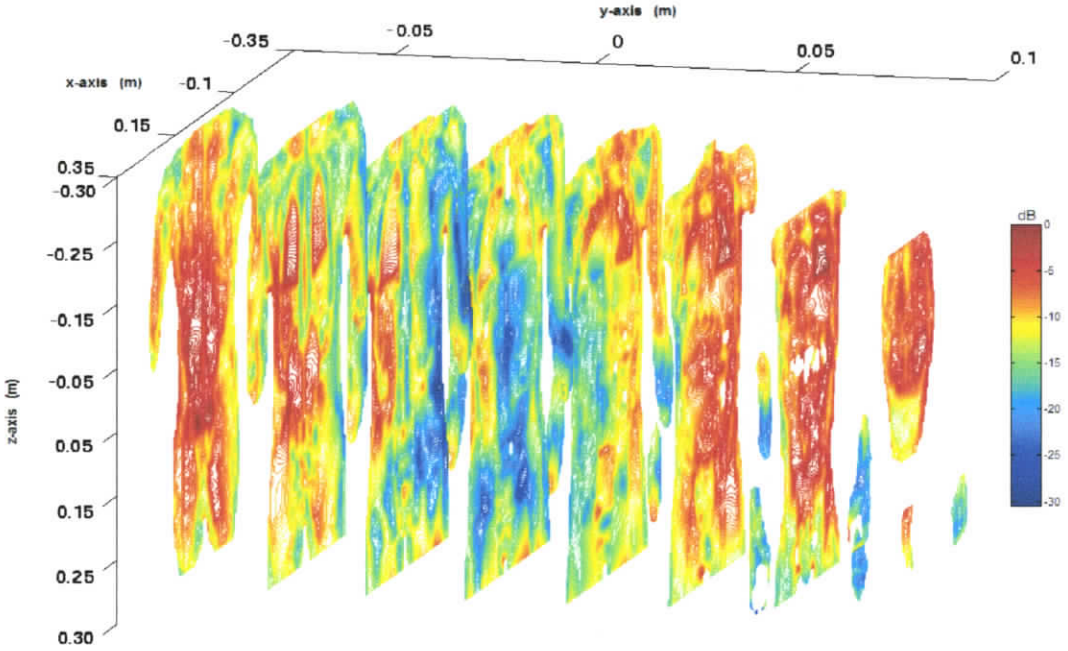

Figure 6-9: Coronal slices of 1g SAR distribution in the torso model in the resonant coil

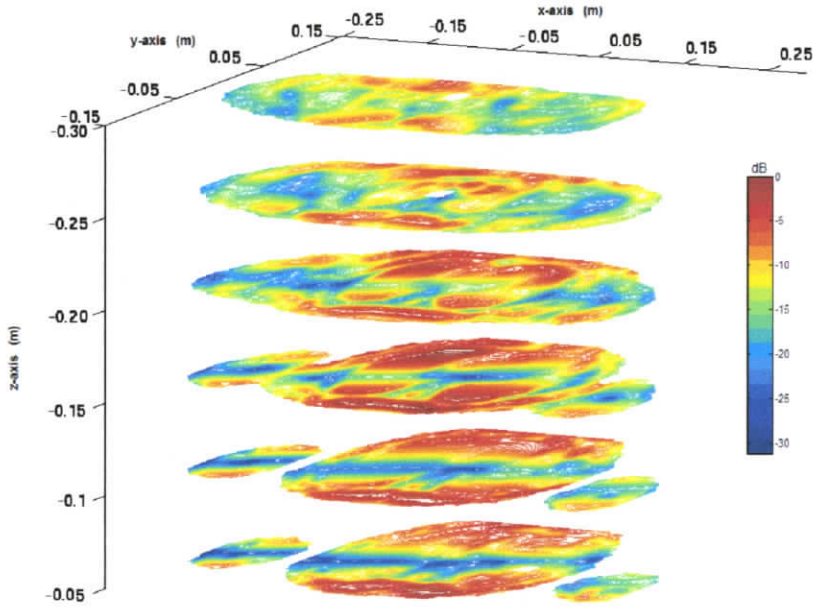

Figure 6-10: Axial slices of 1g SAR distribution in the torso model in the resonant coil

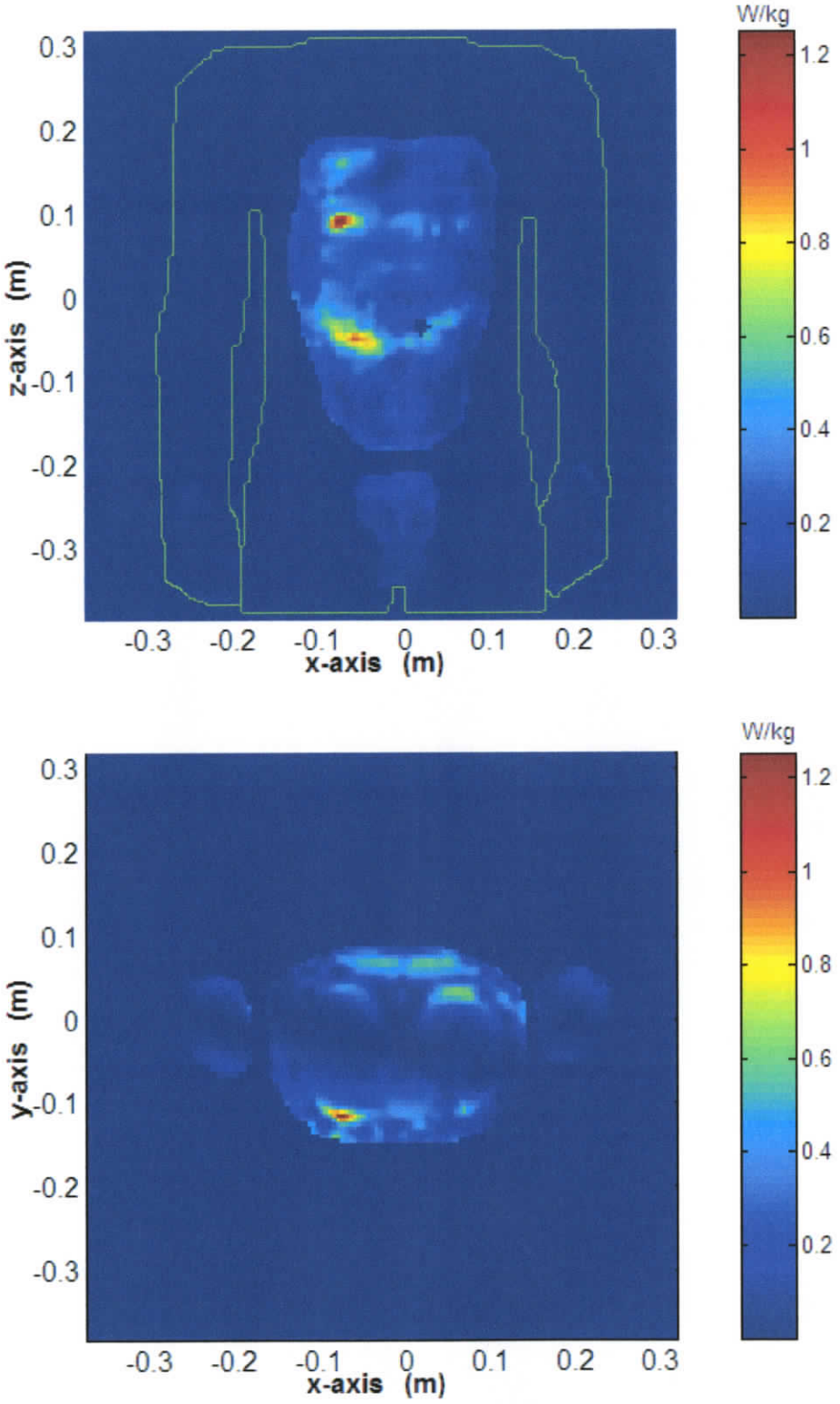

Figure 6-11: Maximum SAR distribution in the torso model for the resonant coil at 64 MHz.

6.3 SAR Enhancement due to Pacemaker

RF electric fields are perturbed by metallic objects; wires in particular can cause significant field enhancements at their ends, bends and any other discontinuities. Additionally, power is deposited in actual conductors (not in perfect conductors). When wires are in biological tissue, they produce higher values of SAR in tissue close to them. The enhancement of SAR values depends on many factors, such as the wire length, diameter, shape and location within the tissue with respect to the unperturbed field.

Figure 6-12 and Figure 6-13 show the 1g SAR differential patterns in the torso model with and without the pacemaker for a non-resonant and resonant coil, respectively. As illustrated, in all cases, enhanced SAR levels are at the end-tips. The relative SAR enhancement is larger for the perfect conductor (PEC) lead than the conductive lead in both coils as no power is lost along its length. Numerical results are given in Table 6-2.

The increase in SAR values computed for the PEC lead is associated with the tip of the lead in both non-resonant and resonant coils. This behavior is not however observed with the conductive lead. Although, enhanced SAR levels are detected at both ends, they are not representative of the maximum SAR values, higher SAR levels are computed elsewhere. Enhanced SAR values of 2.03 W/kg and 0.92 W/kg are computed in proximity of the pacemaker generator in the non-resonant and resonant coil, respectively. The conductive lead is curved and it bends at different angels as it is routed through the veins into the heart. This orientation along with the losses in the lead contributes to enhanced SAR levels along the length of the lead. A rise in SAR of 9.3 W/kg was detected for the conductive lead in the shoulder area (high SAR region) in the non-

resonant coil. No significant rise in SAR was noted in the same location for the resonant coil.

Several studies, [5], [32], [33], and [45], have investigated the SAR and/or heating at tip of wires in human body models. Konings et al. [32], and Nitz et al. [33] measured a rise in temperature at the tip of straight wires in human body models during MRI scans. Using an anatomically correct human body model, Ho [5] calculated the maximum SAR value near the tip of 5 mm radius metallic implant in the heart region in a non-resonant birdcage coil at 1.5 T. The heart area was considered a low SAR region; only a very small SAR increase (0.2 W/kg) in the tissues surrounding the tip of the wire was detected. However, a wire with a radius of 1 mm in the same area produced a higher SAR level (3.1 W/kg). The SAR levels increased significantly when the wires were placed in regions of high SAR at the periphery of the body.

In summary, SAR enhancements due to the pacemaker and its leads are lower for the resonant coil compared to those in the non-resonant coil. This is consistent with lower SAR values in all locations. Also, higher SAR enhancements occur for the leads modeled as perfect conductors.

Table 6-2: 1g SAR enhancement (W/kg) at both ends of the lead–at the generator and at the heart.

	Non-resonant Coil		Resonant Coil	
	at the generator	at the end-tip	at the generator	at the end-tip
Perfect conductor lead	8.94	6.04	0.92	2.78
Conductive lead	1.17	0.56	0.38	0.17

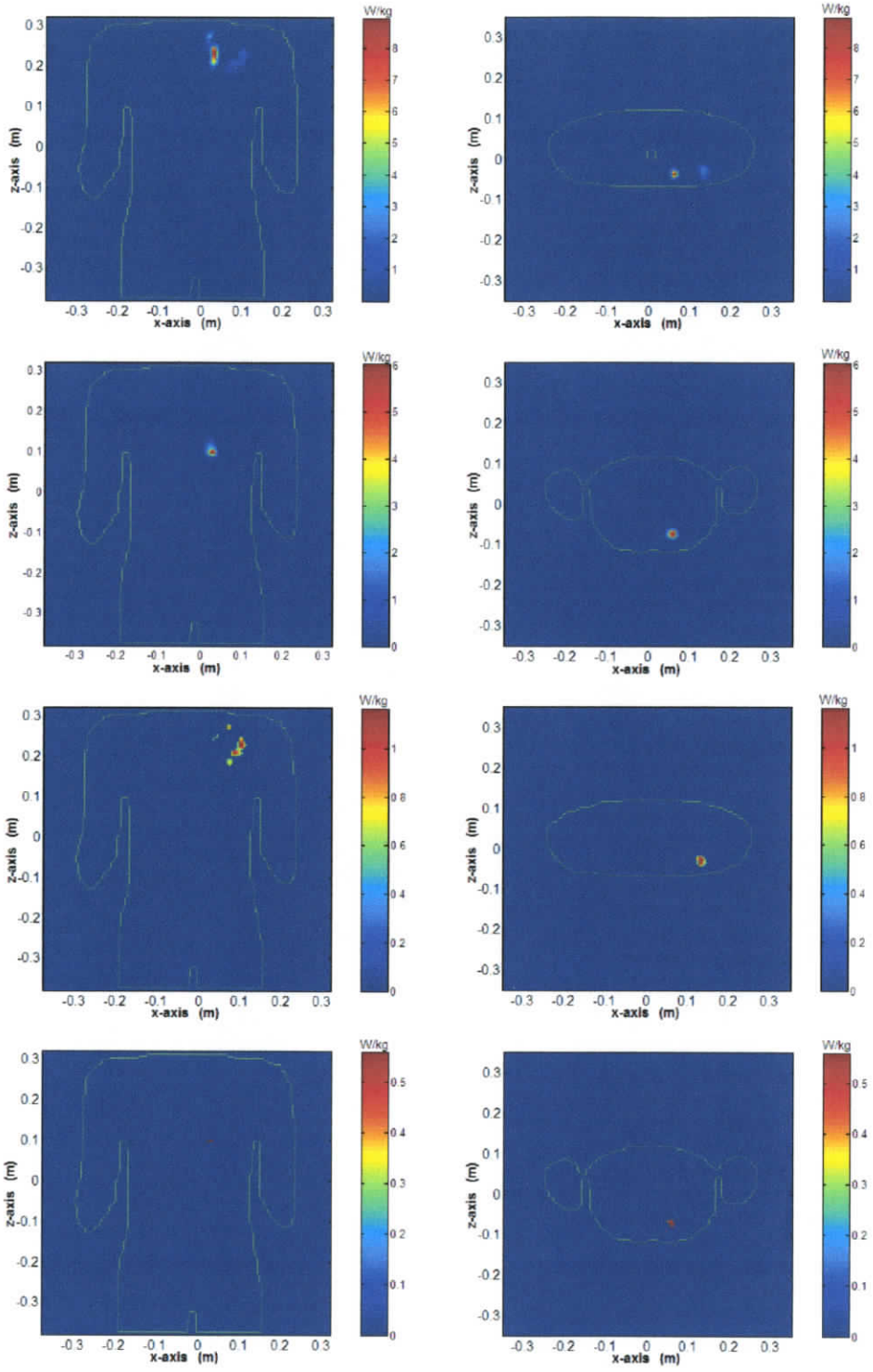

Figure 6-12: SAR (W/kg) at both ends of the pacemaker lead in torso model in the non-resonant coil: top two rows perfect conductor lead, 1st row the generator end of the lead, 2nd row the tip location, and bottom two rows conductive lead, 3rd row the generator end, and 4th row the tip location.

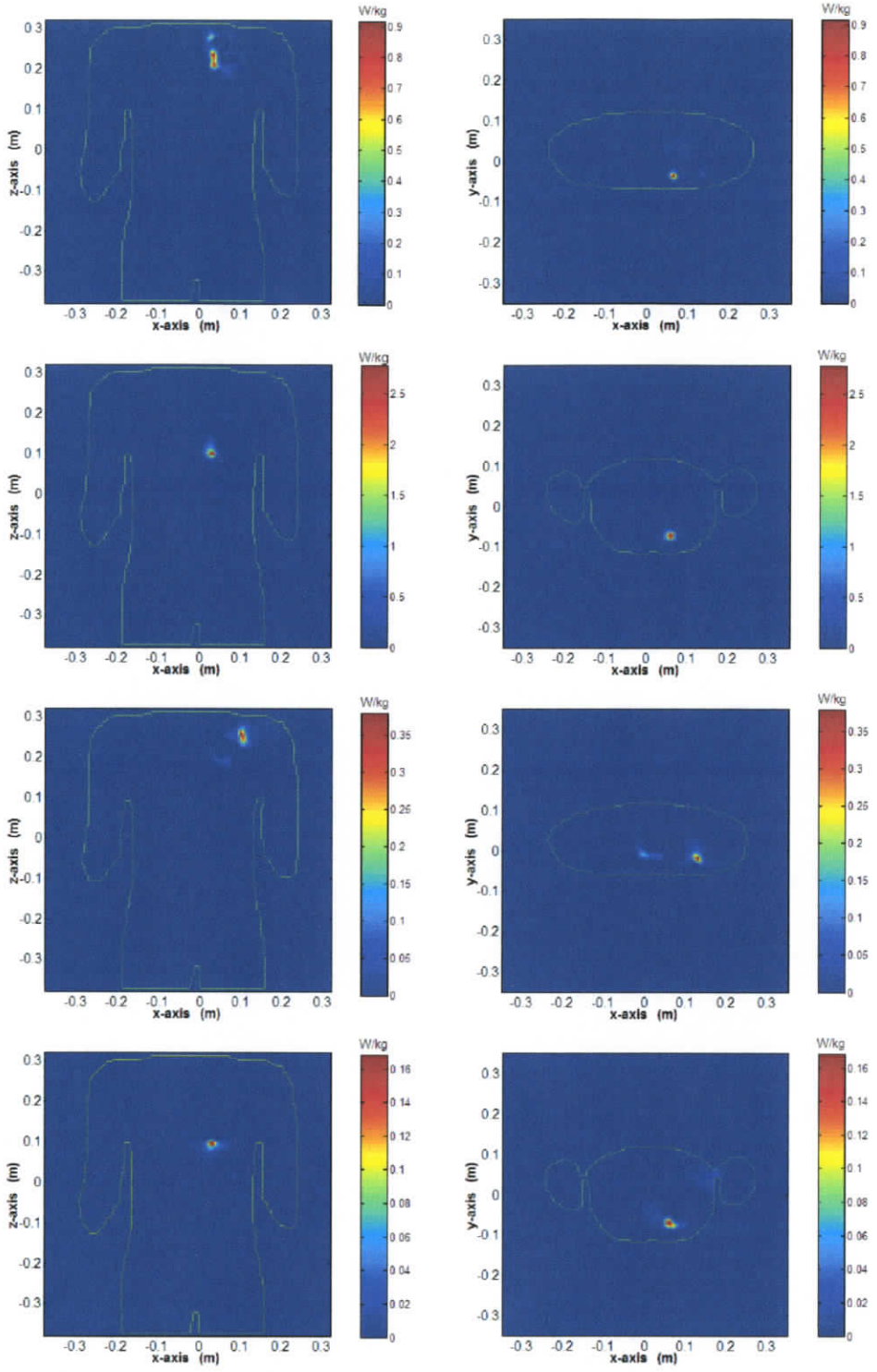

Figure 6-13: SAR (W/kg) at both ends of the pacemaker lead in torso model in the resonant coil: 1st row the generator end of the lead, 2nd row the tip location, and bottom two rows conductive lead, 3rd row the generator end, and 4th row the tip location.

6.4 Organ Dosimetry

The SAR computation in organs and tissues is important in assessing MRI safety. Such data aid in recognizing exposure scenarios for which some of the safety thresholds are exceeded, and evaluating possible biological effects. The human body is inherently heterogeneous, which results in uneven distribution of the absorbed RF energy and SAR in the body. The SAR levels vary depending on the dielectric constant and the conductivity of the tissues and organs.

During an MRI procedure "hot spots" may develop in the internal organs. In this study, the SAR is computed for all the organs and tissues in the torso model with and without the pacemaker. These data provide also an additional outlook on the enhanced 1g SAR levels due to the pacemaker.

Table 6-3 gives the dosimetry data for selected organs for the two RF coils. Where applicable, the relative percent SAR enhancement for each tissue due to the pacemaker is given. Gandhi and Chen [46] computed organ-averaged SAR in an anatomically correct body model with 30 tissues at 64 MHz using a non-resonant whole-body birdcage coil with 16 rungs. Their results along with those from this study are listed in Table 6-4. A comparison of the SAR values in Table 6-4 demonstrates a consistency between the two studies.

In this investigation, the highest 1g SAR level in the non-resonant coil is observed in the skin on the periphery in the high SAR region. Other high SAR values are detected nearby in the muscle and fat tissues. In these "hot spots", the local 1g SAR exceeds the average SAR in the tissues by factors of 18 to 38. In the resonant coil, elevated SAR

values are found in the pectoral cavity. The local 1g SAR levels are found in the lung, fat, muscle, and skin and surpass their average SAR by factors of 9 to 125. As it has been noted previously, the field distribution varies in both coils when the coils are loaded with the torso model. This difference causes the SAR pattern to be considerably different for each coil.

The presence of the pacemaker generator and lead does enhance the local SAR levels in the tissues and organs encompassing them. The heart and lung are the organs in the non-resonant coil where a relative SAR enhancement of 141% and 80% is computed, respectively for the pacemaker and PEC leads. This SAR enhancement is more pronounced in the resonant coil where SAR level increases of about 450% in the heart, 210% in blood, and 157% in fat are observed. The location of the pacemaker generator and lead explain the SAR enhancement in the aforementioned organs and tissues (illustrated in Figure 4.7). The end-tip of the lead is in direct contact with the heart and the generator is placed in the fat tissues in the body model. Due to the varying field distribution in each coil, induced SAR levels in organs and tissues are unique and can not be compared against those in another coil.

One should acknowledge the computational errors in the studies presented. The SAR computations are affected by the size of the Yee cell. The size of the voxel relative to size of the organ or tissue affects the computed results. The inadequate representation of small organs and thin tissues by the given voxel size affect the computed SAR results. As well, when modeling smooth surfaces, staircase approximation introduces errors that may affect the results, especially at the boundary. Such problems could be addressed by

employing human body models of higher resolution. This however would drastically increase the processing time and would require extensive computer resources, which are not currently available to this investigator.

Table 6-3: SAR (W/kg) in various organs and tissue for the human torso model in the resonant and non-resonant coils and the relative enhancement in 1g SAR levels due the pacemaker generator and lead.

Organ	Resonant Coil				Non-Resonant Coil			
	SAR_{AV}	SAR_{1g}	%Enhancement (Conductive lead)	% Enhancement (PEC)	SAR_{AV}	SAR_{1g}	%Enhancement (Conductive lead)	%Enhancement (PEC)
Bladder	0.06	0.37	-	-	0.24	0.99	-	-
Blood	0.09	0.45	66	210	0.40	3.23	195	-
Fat	0.06	0.88	-	157	0.35	11.36	-	0.9
Heart	0.10	0.46	-	446	0.40	2.34	3	141
Kidney	0.10	0.33	-	-	0.53	1.49	-	-
Liver	0.11	0.59	-	-	0.43	1.66	-	-
Lung	0.01	1.25	-	-	0.05	3.74	-	-
Muscle	0.11	1.02	-	-	0.82	15.08	-	0.9
Pancreas	0.05	0.21	-	-	0.44	5.36	-	-
Skin	0.07	0.89	-	-	0.60	16.91	-	0.9
Small Intestine	0.14	0.49	-	-	0.68	2.39	-	-
Spleen	0.10	0.32	-	-	0.64	1.98	-	-
Stomach	0.09	0.33	-	-	0.48	4.37	-	-
Testes	0.05	0.21	-	-	0.44	5.36	-	-
Whole-body	0.09	1.25	-	-	0.63	16.91	-	-

Table 6-4: Comparison of organ averaged SAR levels (W/kg) at 64 MHz

Organ	Non-resonant Coil	
	Present study	Gandhi and Chen[46]
Bladder	0.06	0.03
Blood	0.09	0.11
Heart	0.10	0.10
Kidney	0.10	0.11
Liver	0.11	0.16
Pancreas	0.05	0.06
Prostate Gland	0.05	0.06
Small Intestine	0.14	0.15
Spleen	0.10	0.13

6.5 Summary and Conclusions

The computational procedure was verified by comparing SAR distribution for cylindrical and human torso model with published data. High SAR values were observed near the surface of large models and at the core for the smaller cylindrical models.

The SAR was also evaluated in an anatomically accurate body model with and without a cardiac pacemaker. When loaded with the torso model, the distinct magnetic field distribution in each coil led to different SAR patterns. Although maximum SAR values in both coils were consistently noted in the periphery of the body, the SAR distribution in

each coil was unique. In the non-resonant coil, high SAR levels were noted in the arms near the edges of the coil, where a maximum 1g SAR of 16.9 W/kg was computed. This spatial peak SAR is greater than the corresponding value of 12 W/kg in the extremities given as the limit in FDA guidelines [47]. In the resonant coil, elevated SAR levels were observed in the pectoral and back area of the body. A maximum 1g SAR value of 1.25 W/kg was computed in the pectoral cavity. The high quality factor of the resonant coil resulted in low power dissipation and hence lower SAR levels.

Enhanced SAR levels associated with the cardiac pulse generator and pacing leads are potentially problematic in the surrounding tissues. A considerable rise in the SAR was computed at the end-tips of the PEC lead in the non-resonant coil. An increase in 1 g SAR levels of 8.94 W/kg and 6.04 W/kg were computed at the generator and heart, respectively. The increase in SAR at the generator is above the allowable value of 8 W/kg for the torso as given in the FDA guidelines. SAR levels were significantly lower in the resonant coil; enhanced 1g SAR levels of 0.92 W/kg at the wire and generator interface and 2.78 W/kg at the wire and heart interface were computed. The SAR increases in tissues surrounding the pacemaker generator and lead are well within the safety guidelines.

It was determined that the maximum 1g SAR in the body model with pacemaker was not associated with the tip of the lead, but consistently occurred at the periphery of the body. However, this is in contrast to implants located close to the body surface in high SAR regions.

SAR values in different organs were computed. Average SAR levels were highest in tissues closest to the surface, namely skin and muscle, in the non-resonant coil. The internal organs in and around the pectoral cavity exhibited the highest SAR levels in the resonant coil. The pacemaker generator and lead enhanced the SAR levels in their surroundings. The most notable SAR increase occurred in the heart in both RF coils where the tip of the PEC lead was in contact with the heart.

7 Conclusions

7.1 Thesis Contributions

In this thesis, using numerical modeling, the interactions of the RF fields in MRI with a human body model were investigated. In particular, the interactions of these fields with an implanted pacemaker were studied. The computational procedure was verified by comparison of the magnetic field data and SAR data for simple human models (cylinders) and a human torso model with published data.

The new data obtained in the thesis included:

- The SAR levels in a heterogeneous body model evaluated in two different birdcage coils – a resonant and a non-resonant coil – at a static magnetic field density of 1.5 T (64 MHz).
- The enhancements of the SAR due to an implanted cardiac pacemaker.
- The effect of the conductivity of the pacemaker lead on the SAR levels.

The results of the simulations performed provide an addition to the existing database on safety of MRI procedures. They also further extend understanding of factors influencing the evaluation of RF power deposition during MRI procedures, and more specifically the enhanced SAR values for humans with pacemaker. SAR computations were not previously available for models of pacemakers *in situ*.

7.2 Conclusions

The modeling performed and its comparison with the published data led to the following conclusions with respect to evaluation of the MRI safety for the pacemaker bearers in large birdcage coils operating at 64 MHz:

- Evaluations of the SAR in organs and SAR due to implants performed for non-resonant coils excited in 16 rungs greatly overestimate these values, compared to practical coils employing resonant configurations. Typically, resonant coils produce SAR values that are about 10 times lower than those for non-resonant coils operating with the same magnetic flux density.
- Cardiac pacemaker leads terminate in the heart, where the SAR values are relatively low, and thus the SAR enhancement is relatively low. Thus, evaluation of the SAR enhancement based on wires placed in the body periphery typically gives a gross overestimate.
- Pacemaker leads are not perfect conductors, and modeling them as such, results in much greater 1g SAR enhancements than those produced by actual conductive leads.
- The numerical values of 1g SAR given in this work are for 5 mm diameter pacemaker leads. Thinner leads would result in higher SAR values. While typical leads have a diameter of about 5 mm, they consist of a much thinner wire wound as a helix. The effect of this particular geometry of the lead has not been evaluated.

7.3 Future Work

Further investigations aimed at the MRI safety for the pacemaker bearers can be performed in the following areas:

- Evaluation of the enhanced SAR levels in a high resolution body model for a better accuracy. The further growth in the computational resources makes this task achievable.
- Implementation of the bio-heat equation in the simulation for more realistic results.
- Investigating the SAR enhancements due to broken leads in patients. Although rare, such cases do exist.
- The present trend in MRI is towards higher magnetic fields intensities. The evaluation of the enhanced SAR levels in patients for such systems is therefore important.
- Studying the effect of shielding on SAR levels.
- Evaluation of enhanced SAR in other coils such as phased arrays currently under development.

Bibliography

[1] Sakakibara, Y., Mitsui, T., "Concerns about sources of electromagnetic interference in patients with pacemakers," *Japanese Heart Journal,* 40:737-743, 1999.

[2] Loewy, J., Loewy, A., Kendall E.J., "Reconsideration of Pacemakers and MR Imaging," *Radiographics*, 24: 1257-1267, 2004.

[3] Sommer T, Valhaus C, Lauck G, et al., "MR imaging and cardiac pacemakers: in vitro evaluation and in vivo studies in 51 patients at 0.5 T," *Radiology*, 215: 869-879, 2000.

[4] Nyenhuis, J.A., Kildishev, A.V., Bourland, J.D., Foster, K.S., Graber, G., "Heating near implanted medical devices by the MRI RF-magnetic field," *IEEE Transactions on Magnetics,* 35(5), 4133-4135, 1999.

[5] Ho, H.S., "Safety of metallic implants in magnetic resonance imaging," *Journal MagneticResonance*, 14:472-477, 2001.

[6] Abragam, A., *Principles of Nuclear Magnetism.* Oxford University Press, London. 1961.

[7] Mark A. Brown, Richard C. Semelka. *MRI Basic Principles and Applications.* 3rd Edition. John Wiley and Sons, Inc., Hoboken, New Jersey. 2003.

[8] Catherine Westbrook, Carolyn Kaut. *MRI in Practice.* Blackwell Scientific Publications. Cambridge, Massachusetts. 1993.

[9] Stewart C. Bushong. *Magnetic Resonance Imaging: Physical and Biological Principles.* 3rd edition. Mosby, Inc. 2003.

[10] Jin, J.M., "Electromagnetic Analysis and Design in Magnetic Resonance Imaging", ISBN 0−8493−9693−X, CRC Press, New York, 1999.

[11] Hayes CE, Edelstein WA, Schenck JF, "Radio Frequency Resonators." In *Magnetic Resonance Imaging,* ed. by C.L. Partain, R.R. Price, J.A. Patton, M.V. Kulkarni, A.E. James Saunders, Philadelphia, 1988.

[12] Ackerman, J.J., "Mapping of metabolites in whole animal by 31P NMR using surface coils," *Nature*, 283: 167-170, 1980.

[13] Bendall MR, "Portable NMR sample localization method using inhomogeneous RF irradiation coils," *Chemical Physics Lett*ers, 99: 310-315, 1983.

[14] Ginsberg, D.M., and Melchner, M.J., "Optimum geometry of saddle shaped coils for generating a uniform magnetic field," *Review of Scientific Instruments*, 41: 122-123, 1970.

[15] Hayes, C.E., Edelstein, W.A., Schenck, J.F., Mueller, O.M., Eash, M., "An efficient, highly homogeneous radiofrequency coil for whole body NMR imaging at 1.5 T," *Journal of Magnetic Resonance*, 63: 622-68, 1985.

[16] Leifer, M.C., "Resonant Modes of The Birdcage coil," *Journal of Magnetic Resonance*, 124, 51- 60, 1997.

[17] Ibrahim, T.S., Lee, R., Baertlein, B.A., Yu, Y., Robitaille, P.M.L., "Computational analysis of the high pass birdcage resonator: finite difference time domain simulations for high-field MRI," *Journal of Magnetic Resonance*, 18: 835-843, 2000.

[18] Inan US and Inan AS. Electromagnetic Waves. New Jersey, Prentice Hall. 2000

[19] Shellock FG. Magnetic Resonance Procedures: Health Effects and Safety. New York, CRC Press. 2001.

[20] D. Simunic, P. Wach, W. Renhart, and R. Stollberger, "Spatial distribution of high-frequency electromagnetic energy in human head during MRI: Numberical resutls and measurements," *IEEE Transactions on Biomedical Engineering*, 43: 88-94, 1996.

[21] J.G. Harrison and J. T. Vaughn, "Finite element modeling of head coils for high-frequency magnetic resonance imaging applications," *12th Ann. Rev. Progress in Applied Computational Electromagnetics*, 1220-1226, 1996.

[22] Smith, C.D., Kildishev, A.V., Nyenhuis, J.A., Foster, K.S., and Bourland, J.D., "Interactions of magnetic resonance imaging radio frequency magnetic fields with elongated medical implants," *Journal of Applied Physics*, 87(9), 6188-6190, 2000.

[23] Jin, J.M., Chen, J., Chew, W.C., Gan, H., Magin, R.L., Dimbylow, P.J., "Computation of electromagnetic fields for high-frequency magnetic resonance imaging applications," *Physics in Medicine and Biology*, 41: 2719-2738, 1996.

[24] Ibrahim T.S., Lee R., Baertlein B.A., Kangarlu A., Robitaille P.M.L., "Application of finite difference time domain method for the design of birdcage RF head coils using multi-port excitations," *Journal of Magnetic Resonance*, 18:733-742, 2000.

[25] Ibrahim T.S., Lee R., Baertlein B.A., Robitaille P.M.L., "B_1 field homogeneity and SAR calculations for the birdcage coil," *Physics in Medicine and Biology*, 46: 609-619, 2001.

[26] Nguyen, U.D., Brown, J.S., Chang, I.A., Krycia, J., Mirotznik, M.S., "Numerical evaluation of heating of the human head due to magnetic resonance imaging," *IEEE Transactions on Biomedical Engineering*, 51(8): 1301-1309, 2004.

[27] Chen, J., Feng, Z., Jin, J.M., "Numerical simulation of SAR and B_1-field inhomogeneity of shielded RF coils loaded with the human head," *IEEE Transactions on Biomedical Engineering*, 45(5): 650-659, 1998.

[28] Collins, C.M., Smith, M.B., "Signal-to-Noise Ratio and Absorbed Power as Functions of Main Magnetic Field Strength, and Definition of 90° RF Pulse for the Head in the Birdcage Coil," *Magnetic Resonance in Medicine*, 45: 684-691, 2001.

[29] Collins, C.M., Smith, M.B., "Spatial resolution of numerical models of man calculated specific absorption rate using the FDTD method: A study at 64 MHz in a magnetic resonance imaging coil," *Journal of Magnetic Resonance*, 18: 383-388, 2003.

[30] Collins, C.M., Smith, M.B., "Calculations of B_1 Distribution, SNR, and SAR for a Surface Coil Adjacent to an Anatomically-Accurate Human Body Model," *Magnetic Resonance in Medicine,*, 45: 692-699, 2001.

[31] Chou, C.K., McDougall, J.A., and Chan K.W., "RF heating of implanted spinal fusion stimulator during magnetic imaging," *IEE Transactions on Biomedical Engineering*, 44(5), 367-373, 1997.

[32] Konings, M.K., Bartels, L.W., Smits K.F.M., Bakker, C.J.G., "Heating around intravascular guidewires by resonating RF waves," *Journal of Magnetic Resonance*, 12:79-85, 2000.

[33] Nitz, W.R., Oppelt, A., Renz, W., Manke, C., Lenhart, M., Link, J., "On the heating of linear conductive structures as guide wires and catheters in interventional MRI," *Journal of Magnetic Resonance*, 13:105-114, 2001.

[34] Park, S.M., Nyenhuis, J.A., Smith, C.D., Lim, E.J., Foster, K.S., Baker, K.B., Hrdlicka, G., Rezai, A.R., Ruggieri, P., Sharan, A., Shellock, F.G., Stypulkowski, P.H., Tkach, J., "Gelled versus nongelled phantom material for measurement of MRI-induced temperature increases with bioimplants," *IEEE Tranactions on Magnetics*,39(5): 3367-3371, 2003.

[35] Shellock, F.G., "Metallic neurosurgical implants: evaluation of magnetic field interactions, heating, and artifacts at 1.5-Tesla," *Journal of Magnetic Resonance*, 14: 295-299, 2001.

[36] Achenbach, S., Moshage, W., Diem, B., Schibgilla, V., and Bachmann, K., "Effects of magnetic resonance imaging on cardiac pacemakers and electrodes", *American Heart J*ournal, 134(3), 467-474, 1997.

[37] Ibrahim TS, Lee R, Baertlein BA, Yu Y, Robitaille PML. "Computational analysis of the high pass birdcage resonator: finite difference time domain simulations for high-field MRI", *Journal of Magnetic Resonance*, 18: 835-843, 2000.

[38] Taflove A, Hagness SC. Computational electrodynamics: the finite-difference time-domain method. Artech House: Dedham, MA., 1995.

[39] Yee, K.S., "Numerical solution of initial boundary value problems involving Maxwell's equations in isotropic media", *IEEE Transactions on Antennas and Propagation, 14(5):*302-307, 1966.

[40] Kunz, K.S., Luebbers, R.J., The Finite Difference Time Domain Method for Electromagnetics. CRC Press, Boca Raton, FL., 1993.

[41] Berenger, J.P., "A perfectly matched layer for the absorption of electromagnetic waves", *Journal of Computational Physics*, 114:185-200, 1994.

[42] Sullivan DM, Electromagnetic Simulation using the FDTD Method. New York, NY: IEEE Press: 2000.

[43] Vaughan, J,T., Hetherington, H.P., Otu J.O., Pan, J.W., Pohost, G..M.., "High frequency volume coils for clinical NMR imaging and spectroscopy," *Magnetic Resonance in Medicine,* 32: 206-218, 1994.

[44] Collins, C.M., Smith, M.B., "RF fields induced during MRI in a heterogeneous human head model," *Proc. IEEE 24th Ann. Northeast Bioengineering Conference* 29-31, 1998.

[45] Yeung, C.Y., Susil, R.C., Atalar, E.,"RF safety of wires in interventional MRI: Using a safety index," *Magnetic Resonance in Medicine,* 47: 187-193, 2002.

[46] Gandhi, O.P., Chen, X.B., "Specific absorption rates and induced current densities for an anatomically-based model of the human for exposure to time-varying magenetic fields of MRI," *Magnetic Resonance in Medicine,* 41: 816-823, 1999.

[47] http://www.fda.gov/cdrh/ode/guidance/793.pdf